Coastal Engineering 190 (2024) 104487

Contents lists available at ScienceDirect

Coastal Engineering

journal homepage: www.elsevier.com/locate/coastaleng

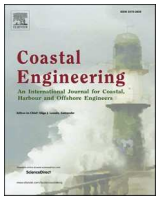

Measuring hydrodynamics and exploring nearshore processes using distributed sensing of fiber-optic cable strain

H.E. Glover [a,*], M.E. Wengrove [a,**], R. Holman [b]

[a] College of Engineering, School of Civil & Construction Engineering, Oregon State University, 101 Kearney Hall, Corvallis, OR, 97331, USA
[b] College of Earth, Ocean, and Atmospheric Sciences, Oregon State University, 104 Ocean Admin Building, Corvallis, OR, 97331, USA

A B S T R A C T

Distributed Acoustic Sensing (DAS) is a new method for recording oceanographic processes using seafloor fiber-optic cables, such as telecommunication cables. DAS returns spatially distributed measurements of cable strain, which can be related to hydrodynamic pressure, turning a submarine cable into a dense sampling array. A reinforced fiber-optic cable was installed in the cross-shore from the dune toe to ~15-m-water depth at the USACE Field Research Facility in Duck, NC to quantitatively compare DAS strain to co-located pressure sensors. We develop a methodology for transferring DAS strain to dynamic pressure and evaluate the performance of DAS to measure shallow- and intermediate-water waves in the incident band (0.04–0.4 Hz). A frequency-dependent empirical transfer function from DAS strain to dynamic pressure at the seabed is derived from the ratio of strain and pressure power spectra. DAS-derived significant wave heights and peak periods were consistent with pressure sensors (typical rmse = 0.2 m and 1 s) over a wide range of dynamic conditions (0.24–4 m wave heights and 3–18 s periods). DAS data were input into the cBathy algorithm to calculate cross-shore bathymetric profiles and were used to calculate cross-shore wave reflection. Preliminary applications of DAS to record wave splitting and shoreline position were explored. With this field data, we demonstrate new applications of DAS for measuring nearshore processes and encourage further exploration. The promising potential of DAS lies in the near-bed data volume provided, real-time capability, and ability to sample in any weather or light.

1. Introduction

In-situ observation of nearshore hydrodynamic and geomorphic processes is fundamentally important for predicting shoreline change and storm impacts (Chardón-Maldonado et al., 2016a; Gomes da Silva et al., 2020; Holman and Haller, 2013), tracking pollutants (Boehm et al., 2017), and predicting rapid-onset hazards like sneaker waves and rip currents (Dalrymple et al., 2011). These processes operate and evolve over a wide range of spatial and temporal scales, which can be challenging to capture in traditional instrument records without assimilating many data streams (Holman and Haller, 2013; Wilson et al., 2014). Ideally, *in-situ* measurements of the nearshore should be collected across a comparably wide range of scales.

Distributed Acoustic Sensing (DAS) is a rapidly expanding measurement technique with the potential to measure near-bed, nearshore processes at a wide range of spatial resolutions using existing fiber-optic cables, such as telecommunication or power cables that contain a fiber for data transmission. A DAS interrogator turns a fiber-optic cable into an array of strain sensors by measuring the phase-shift in reflected light from a laser. This technology has already been widely applied in onshore and offshore seismology, stratigraphy, and the oil and gas industry (Jousset et al., 2018; Lindsey and Martin, 2021; Mateeva et al., 2014; Spica et al., 2020, 2022). Oceanographic applications for DAS have been expanding, and recent work has demonstrated that submarine DAS strain records distant storms (Bouffaut et al., 2022; Landrø et al., 2022) and surface gravity waves (Lindsey et al., 2019; Smith et al., 2023; Williams et al., 2019, 2022). Here we present novel findings from the first applications of DAS to measure nearshore waves and bathymetry.

Historically, *in-situ* observations of surface waves were primarily collected by deploying individual, fixed or free-floating sensors to measure water pressure, sea surface elevation or slope, and/or water velocity. Logistical challenges and cost limit the spatial and temporal resolution of point sensor deployments, especially in energetic or extreme environments (Streβer et al., 2022). Yet, capturing measurements during storm events and in energetic regions is critical for theory and model development (O'Grady et al., 2019; Senechal et al., 2011). Measurements in the swash zone are especially important for understanding the physical drivers of wave runup and total water level, TWL (Gomes da Silva et al., 2020). However, these *in-situ* instruments can interfere with flow in the swash zone, altering the fundamental processes of interest (Chardón-Maldonado et al., 2016b). Similar logistical and safety constraints have also limited direct measurements of

* Corresponding author.
** Corresponding author.
E-mail addresses: gloverha@oregonstate.edu (H.E. Glover), Meagan.Wengrove@oregonstate.edu (M.E. Wengrove).

https://doi.org/10.1016/j.coastaleng.2024.104487
Received 8 September 2023; Received in revised form 13 February 2024; Accepted 14 February 2024
Available online 19 February 2024

associated, nearshore bathymetry. Historically, bathymetric measurements have been made with amphibious or shallow-water vessels equipped with sonar systems (Anderson et al., 2023; Holman et al., 2013).

More recently, remote sensing methods have significantly expanded, providing new ways to generate 2D arrays of measurements. Nearshore hydrodynamics and bathymetry can be recorded from cameras (Buscombe et al., 2010; Carini et al., 2015; Holman et al., 2013; Holman and Bergsma, 2021; Martins et al., 2023; Palmsten and Holman, 2012; Splinter et al., 2018), radar (Ardhuin et al., 2019; Bell, 1999; Hauser et al., 2023; Holman and Haller, 2013; Honegger et al., 2019), and lidar (Almeida et al., 2020; Brodie et al., 2017, 2015; Carini et al., 2021; O'Dea et al., 2019). These remote-sensing techniques all target the ocean surface, providing only inferred information about near-bed processes. Such techniques are also often limited by weather or light conditions, which inhibit data collection during both energetic storms and extremely calm conditions with minimal foam or surface roughness. Furthermore, these techniques are generally limited to a cross-shore spatial range of 100s of meters for lidar and imagery, and kilometers for radar.

DAS has recently demonstrated promising potential for supplementing existing, nearshore observational techniques, providing significant spatial and temporal resolution for near-bed measurement at limited cost. DAS data can be collected along a submarine cable at kilohertz frequencies with meter-scale spacing over 10s–100s of kilometers, providing 1000s of sampling locations. Surface waves have been reported in DAS datasets collected on the continental shelf (Lindsey et al., 2019; Williams et al., 2019, 2022) and recent work has demonstrated that there is a positive relationship between cable strain and wave height (Taweesintananon et al., 2023; Williams et al., 2022). However, quantitative relationships between strain and hydrodynamically relevant parameters (e.g., pressure and bed shear stress) have yet to be developed, and the full capabilities of DAS as an oceanographic measurement technique have not been explored.

The goal of this paper is to quantify, ground-truth, and explore hydrodynamic signals in DAS strain data collected on a fiber-optic cable during a three-month-long experiment at the U.S. Army Corps of Engineers' Field Research Facility (FRF) in Duck, North Carolina. DAS strain data was collected along a 1.5 km long cross-shore cable and compared against robust point and array measurements of nearshore hydrodynamics and bathymetry. This combined dataset is used to:

1. Provide methodology for and validate an empirical transfer function for converting DAS strain to dynamic pressure;
2. Validate applications of the DAS-derived pressure data for calculating bulk wave statistics, calculating wave-reflection, and extracting bathymetry; and
3. Explore a range of nearshore processes recorded by DAS.

2. Theory behind submarine Distributed Acoustic Sensing

DAS takes advantage of the natural Rayleigh backscatter of light in single-mode optical fibers. The glass in fiber-optic cables contains random impurities that generate an unknown but relatively uniform field of weak-backscatter sources. A DAS interrogator emits short laser pulses with a known length and shape and measures the phase difference of signals reflected from the field of impurities. Changes in the phase are linearly related to the cable strain, where strain is the fractional change in cable length over a known reference distance, called the gauge length. The gauge length is limited by the characteristics of the interrogator and the laser-pulse length, with typical values in the range of 2–20 m. This method is called phase-sensitive optical time-domain reflectometry (Φ-OTDR). DAS interrogators can output either strain or strain rate, depending on the exact interferometric method used. Either technique provides a record of nanoscale, longitudinal strain at 100s–1000s of user-defined points along a cable.

The along-cable resolution of the strain field is fundamentally the gauge length, however strain can be recorded at user-defined intervals, called channels, to reduce data storage or improve the signal-to-noise ratio (SNR). The SNR can be improved by stacking measurements from adjacent channels. This stacking reduces the probability of signal loss due to optical fading effects (Lindsey and Martin, 2021), which are spatially static patterns generated by interference between scatterers. Channel locations are uniformly spaced along the cable and are defined by the distance from the interrogator. Geolocating channels requires the input of an identifiable signal at a known location (colloquially called tap-testing, Peng et al., 2023).

When a surface gravity wave propagates across the ocean surface it imposes a pressure gradient on the seafloor in shallow and intermediate water depth conditions. The pressure at the bed can be partitioned into a hydrostatic component, p_0, and a dynamic component, p',

$$p = p' + p_0 = \frac{\rho g a \cos(kx - \omega t)}{\cosh(kh)} + \rho g h. \quad (1)$$

Dynamic and hydrostatic pressure can be respectively represented by the corresponding terms on the RHS, where ρ is water density, g is gravity, a is the wave amplitude, k is the wavenumber, h is the water depth, and ω is the wave frequency. Pressure gradients impose an implied strain on the seabed. The DAS interrogator records the total, integrated cable strain over the gauge length (Fig. 1), imparting a wavelength dependence. In essence, the strain response will vary depending on the ratio between wavelength and gauge length (Martin, 2018; Vantassel et al., 2022), where a wave with the same wavelength as the gauge length would impart net-zero integrated strain (Fig. 1). The recorded strain will also vary based on the relationship between water depth and wavelength (Eqn. (1)), as the wave-induced dynamic pressure decays as cosh(kh). A deep-water wave would impart no direct strain due to dynamic pressure on the cable (Taweesintananon et al., 2023). Additionally, the measured strain will decay as cos(θ), where θ is the angle between the cable and the wave ray (Hubbard et al., 2022; Martin, 2018; Taweesintananon et al., 2021). A wave propagating normal to the along-cable direction would impart no along-cable strain, assuming the wave crest is longer than the gauge length. The recorded strain will also depend on the seafloor compliance, the cable compliance, the cable temperature, and the characteristics of the transmitted laser pulse (Hubbard et al., 2022; Reinsch et al., 2017; Williams et al., 2022).

All of these factors must be addressed when quantifying pressure and

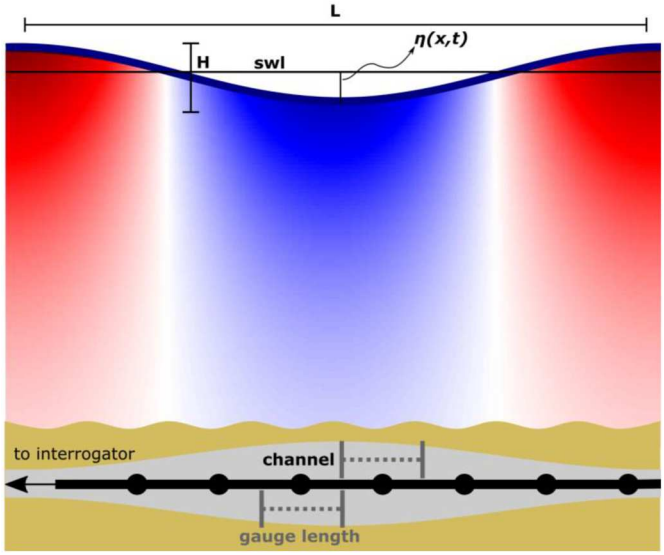

Fig. 1. Diagram of a submarine fiber-optic cable under a surface gravity wave. The colormap shows the dynamic pressure, or variation in pressure from hydrostatic pressure. This cartoon is not shown to scale.

wave parameters using DAS strain. Thus, an analytical transfer function between strain and dynamic pressure under a wave would require *a piori* knowledge of the cable composition, bed material, burial depth, and water temperature over the entire deployment at each channel location. The focus of this study was to instead develop an empirical calibration between dynamic pressure at the seabed and DAS-measured strain, based on co-located measurements of seabed strain and dynamic pressure in the field (Fig. 2). The calibration accounts for the relationship between wavelength and DAS-measured strain by comparing power-spectral density in frequency space and calculating a frequency-dependent correction from DAS-measured strain to near-bed dynamic pressure. For linear waves, frequency and wavelength are related by the dispersion relation ($\omega^2 = gk\tanh(kh)$, where ω is wave frequency, g is gravity, k is wavenumber, and h is water depth). This calibration method assumes that the dominant strain signal in the incident wave band (0.04–0.4 Hz) is the dynamic pressure (Eqn. (1)).

Here, the correction factor C is calculated as,

$$C(x,f) = \frac{P(x,f)}{E(x,f)} \tag{2}$$

where $C(x,f)$ is the frequency-dependent correction factor at channel x, $P(x,f)$ is the PSD (power spectral density) of pressure measured near channel x, and $E(x,f)$ is the PSD of strain at channel x. This correction factor inherently incorporates the impacts of seafloor compliance, cable compliance, the shape of the transmitted laser pulse (Hubbard et al., 2022; Reinsch et al., 2017), and the relationship between gauge length and wavelength (Fig. 1). The accuracy of this method is evaluated using field data collected at the USACE Field Research Facility.

3. Study site and methods

3.1. Field site

The US Army Corps of Engineers Field Research Facility (FRF), provides an ideal location for developing new, nearshore measurement techniques. USACE maintains instrumentation to monitor nearshore processes using both point-instruments and remote sensing techniques (USACE, 2023 https://frfdataportal.erdc.dren.mil/), providing robust ground-truth for evaluating new methods. The facility encompasses ~1 km of linear beach backed by vegetated dunes, located on a barrier island near Duck, North Carolina. The tidal range is ~1 m. The beach is primarily composed of mixed fine and coarse sand with a $D_{50} \sim 0.2$ mm, and the average foreshore slope is ~1:12 (Birkemeier et al., 1981; Plant et al., 1999). There is a ubiquitous offshore bar or set of bars that migrates seasonally between an offshore position of ~100–300 m (Anderson et al., 2023).

3.2. Field data collection

A 1700-m-long segment of reinforced fiber optic cable was deployed on November 3, 2021 along the northern boundary of the FRF (yFRF = 985 m, Fig. 2). The cable was a 9.4 mm OD Single Armor Umbilical with two single-mode and two multimode, tightly buffered fibers inside a gel-filled steel tube, covered in plastic and surrounded by a spiral of steel wire with a plastic sheath. The cable had a specific gravity greater than that of sand. A spool of the fiber was staked and buried in the dune toe, and the cable was trenched into the beach to the waterline. The submarine portion of the cable was laid from an amphibious vehicle, and

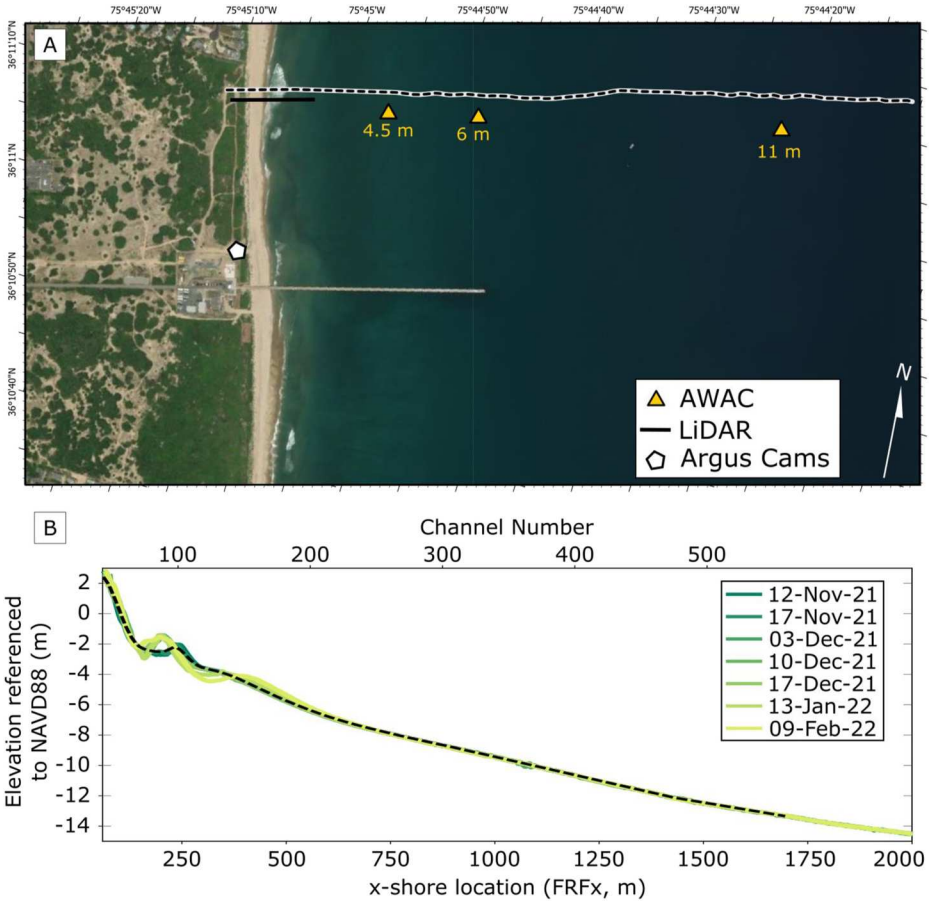

Fig. 2. Overview of field site and instrument locations. A) Map of the FRF facility with relevant instrument locations and cable path. B) Bathymetric cross-sections at the cable location (yFRF = 985 m) collected by the LARC throughout the study period. The initial cable deployment profile is shown with a black, dashed line.

the cable weight promoted self-burial.

DAS data were collected from 3-Nov-2021 to 10-Feb-2022 with a Sintela Onyx interrogator sampling at 20 kHz with a 4.8 m gauge length and 3.2 m channel spacing (552 channels). Data files were saved at 500 Hz in 17-min segments, for an individual file size of ~1.14 GB and a total of ~10 Tb of data. Sample time was continuously synched to GPS time. Channel locations were calibrated based on the passage of a vehicle over the buried cable (see Figs. S1–S2 for more details). Unfortunately, a kink in the cable was introduced during the deployment process around channel 143 (xFRF ~ 400 m); this kink impacted measurements of signal in the frequencies lower than 0.07 Hz offshore of channel 143 periodically from 9-Nov onwards and permanently from 12-December onwards.

Ground-truth measurements of hydrodynamics and morphology were provided by the FRF (https://frfdataportal.erdc.dren.mil/). Three Nortek Acoustic Wave and Current profilers (AWACs) are permanently deployed at 4.5 m, 6 m, and 11 m water depths (Fig. 2), which provide bulk wave parameters and current measurements at hourly intervals. The published bulk wave parameters are calculated using pressure, velocity, and surface tracking (Nortek, 2022). These instruments also record the raw pressure at 2 Hz for 107 min starting every other hour. Unfortunately, the AWAC clocks are not continuously synched to GPS time, and the internal drift is ~60 s per year (Nortek, 2022). Additionally, the exact distance between the AWACs and each DAS channel was not known. Consequently, it was not possible to make direct, time-series comparisons between strain and pressure. Instead, the pressure spectra were compared against the DAS strain spectra from the same 30-min window.

Bathymetric surveys have been conducted at the FRF on a monthly to biweekly basis since 1981 using amphibious vehicles (Forte et al., 2017). Additionally, nearshore bathymetry is derived during daylight hours from the application of cBathy to Argus camera array imagery collected every half hour (Palmsten and Brodie, 2022).

3.3. Data processing

The principle focus herein is the ability of DAS to measure near-bed, dynamic pressure and calculate the characteristics of the nearshore wave field (i.e., wave height, period, and spectrum). This analysis is the focus of Sections 3.3.1, 4.2, and 5.1. The evaluated DAS wave array provides an opportunity to explore additional nearshore dynamics. Thus, we also test cBathy predictions, wave reflection estimates, and show some DAS capabilities for measuring wave non-linearities, wave breaking, and estimates of shoreline position (Sections 3.3.2–3.3.4, 4.2, and 5.2). While these examples represent powerful applications, the latter studies are exploratory rather than exhaustive.

3.3.1. Calculating strain and the empirical correction factor

For each DAS channel, the raw phase was detrended with a 9-min moving average to decrease low-frequency signals likely related to temperature fluctuations in both the cable and the interrogator (Sidenko et al., 2022). Strain was then calculated from optical phase following the standard, linear method described in Lindsey and Martin (2021),

$$\varepsilon = \frac{\lambda \Delta \Phi}{4\,\pi\, n\, gl\, \Psi} \tag{3}$$

where ε is cable strain (m/m); λ is the light wavelength (1550.12e-9 m); $\Delta\Phi$ is the change in phase recorded by the DAS (rad.); n is the fiber index of refraction (1.46);ψ is Pockel's coefficient for single-mode fiber glass (ψ = 0.79); and gl is the gauge length (4.8 m). The DAS records were then decimated to 2 Hz and compiled by day for efficient processing. Decimation was accomplished by first applying a low-pass, zero-phase Butterworth filter with a cutoff frequency of 4 Hz and then selecting every 250th sample. This sample frequency is comparable with imagery techniques, like Argus, which provide efficient yet robust signal-processing resolution (Holman et al., 2013).

DAS-derived pressure at the seabed was calculated by empirically calibrating strain at each channel to pressure recorded by the nearest AWAC. The pressure and strain PSD spectra were calculated using Welch's method for 30-min segments with 512-sample, 50%-overlapping Hanning windows. The correction factor C was calculated as in Eqn. (2). Any given spectrum has uncertainty, leading to variability in the C ratio. The ratio also varied as cable burial depth changed. The cable buried during a storm from 5-Nov to 9-Nov resulting in greater strain signal after burial, likely related to associated seafloor coupling (Figs. S3–4). Consequently, the correction factor varied in time, and a temporal median was taken to generate a single correction for each channel using only data after the storm.

The accuracy of the DAS calibration was evaluated by calculating incident-band wave parameters from the spectra of AWAC pressure and DAS-derived pressure in the frequency range from 0.04 to 0.4 Hz. Significant wave height, H_s, was calculated as $4\sqrt{m_0}$, where m_0 is the zeroth moment of the spectrum. Peak period, T_p, was calculated as the inverse of the frequency of the peak of the spectrum. Energy-weighted average period, T_e, was calculated as the inverse of the energy-weighted frequency ($T_e = \frac{1}{f_e}, f_e = \frac{\sum Ef}{m_0}$), which more accurately represents the energy of the wave field. The fit and rmse were calculated for each wave parameter at each channel using k-fold cross-validation. Cross-validation is a robust method to evaluate the performance of a model using multiple subsets of calibration data and withheld testing data. Here, the performance was evaluated from the average of 10 subsets of calibration and testing data. For reference, the bulk wave parameters published by the FRF from the AWACs are also included, which were calculated using pressure, velocity, and surface tracking (PUV, Nortek, 2022). The impacts of the length of the calibration period, distance between channel and AWAC, and time from initial calibration were also evaluated. However, for the additional analyses below, DAS-derived pressure was calculated using the median, frequency-dependent correction factor derived for each channel from the nearest AWAC.

3.3.2. Wave reflection

The DAS-derived pressure was used to calculate a wave reflection coefficient centered on each channel. Incident and reflected waves were separated using two methods: the pressure-array method for waves propagating over a sloping bed (Baldock and Simmonds, 1999; Inch et al., 2016, 2017a) and the Radon Transform (Almar et al., 2014). For the array method, shoreward and seaward wave trains were separated using the pressure at five DAS channels, spaced five channels apart (16-m spacing), for 30-min segments. Channel spacing was selected to avoid integer multiples of half the wavelength to reduce reflection calculation errors (Lin and Huang, 2004). For the Radon Transform method, the entire DAS array was used in 30-min segments. The reflection coefficient, K_r, was calculated as the square root of the ratio of outgoing to incoming energy flux, which was calculated from the separated wave spectra at each channel. A value of 1 would indicate total wave reflection and 0 would indicate no wave reflection. The 15 channels around the kink were removed from the analysis to avoid noise produced by erroneous strain measurements. All other channels were included. Wave reflection coefficients were also calculated at each of the AWAC locations using the cross-correlation between pressure and cross-shore velocity (Huntley et al., 1999; Sheremet et al., 2002).

3.3.3. cBathy

The DAS-derived pressure was used to calculate a bathymetric profile using the cBathy algorithm (Holman et al., 2013). The cBathy algorithm is designed to operate with a 2D data grid, and two methods were explored for adapting the algorithm to work with linear DAS data. For the first method, the DAS data was artificially replicated at ten, parallel, alongshore locations, centered on the actual cable location, to create an artificial 2D grid of strain. For the second method, the cBathy algorithm was linearized to operate in 1D, eliminating considerations of wave

angle (herein called Linear cBathy). Note that cBathy needs at least five cross-shore datapoints per wavelength for accurate calculation of bathymetry. With 3.2 m channel spacing, we can resolve down to ~16 m wavelength waves, which is close to the limit of relevant frequencies (period ~ 4 s). Pressure was input to cBathy in 20-min segments and the results for each hour (3 runs) were Kalman filtered using the functions built into the cBathy toolbox (Holman and Bergsma, 2021). The bathymetry was also calculated from the standard Argus camera imagery for the corresponding time periods with Kalman filters.

3.3.4. Shoreline position

Finally, the cross-shore DAS strain gradient was used to estimate the shoreline position of the Total Water Level (TWL), which is the sum of all contributions to the water elevation at the coastline. The main contributions to TWL are mean sea level, tides, storm surge, and wave setup and runup (Mull et al., 2014; O'Grady et al., 2019; Ruggiero et al., 2001a; Serafin et al., 2019). At the FRF, a fixed lidar system is used to record TWL at 7 Hz for 30 min periods (O'Dea et al., 2019). The average gradient of the strain magnitude between adjacent channels was calculated at the xFRF shoreline position measured by the lidar on 12-Nov. This gradient value was significantly greater than the average, in-water strain gradient and was used to identify the channel position of the shoreline using the along-cable strain gradient at all times in the DAS record. The DAS-derived shoreline was low-pass filtered at 60 min for comparison with the lidar-derived shoreline position. Considering the 3.2 m spatial resolution of the DAS channels, these shoreline estimates are only presented in the Supporting Information (Text S1).

4. Results

4.1. The relationship between nearshore wave conditions and DAS strain signals

During the deployment period, significant wave height varied between 0.24 and 4.0 m (Fig. 3B), and the peak period varied between 3 and 18 s (Fig. 3C). The cross-shore direction at the FRF is nominally 72° from North, and waves arrived between 30 and 126° (<54° to shore, Fig. 3D). The largest storm event occurred at the beginning of the deployment, on November 6–9th with a maximum significant wave height of 4 m at ~10 s period.

Onshore propagating waves were recorded in the DAS measurements as bands of compression and extension (Fig. 4A). Strain magnitude generally increased over the shore parallel sandbar (xFRF = 200–300) and in the wave-breaking region at the shoreline (xFRF = 95–120). The cross-shore profile of DAS also captured the reduction in strain magnitude at the waterline. Strain magnitude decreased at non-uniformly spaced channels due to optical fading and the cable kink at xFRF~400 m. In f-k space, the DAS strain recorded energy propagating onshore (positive frequencies) and offshore (negative frequencies) (Fig. 4B). Energy was concentrated along the curves predicted by the dispersion relation for the water depths in this example (2.5–12 m). The energy content of the incident frequency bands for the strain and the pressure were consistent between adjacent channels and AWACs (Fig. 4C and D). Example DAS time-stacks look remarkably similar to those of the ground truth AWACs (Fig. 4), revealing the spectral details of wave energy changes over time. The ratio of the two spectral time-stacks also shows the frequency dependence of DAS strain, consistent with the theory we present in Section 2, as well as some variation with time (Fig. 4E).

4.2. Empirical calibration of DAS strain to pressure

The empirical correction equation (Eqn. (2)) was evaluated from spectra of pressure and strain, as demonstrated for the three channels nearest the AWACs (Fig. 5A–F). The shape of the correction factor remained constant throughout the calibration period and is on the order of 10e9 in magnitude. In the incident band, the correction factor decreases with increasing frequency and varies over an envelope of values of 1e9 with the spread consistently lower in the frequency bands containing the dominant energy. The temporal median of the correction factor captured this shape and magnitude while reducing the influence of outliers at any given frequency. Sources of outlying calibration ratios are described in the Discussion.

The DAS-derived pressure was used to calculate bulk wave statistics (Fig. 5 G–L). The DAS-derived wave statistics for November are consistent with the published values from the AWACs (PUV method) and with wave statistics calculated from the AWAC pressure spectra alone (Table 1). For the three channels nearest each AWAC, the R^2 and rmse are 0.84–0.88 and 0.21–0.63 m, respectively, for significant wave height, evaluated against the AWAC-pressure wave statistics (Fig. 6). For

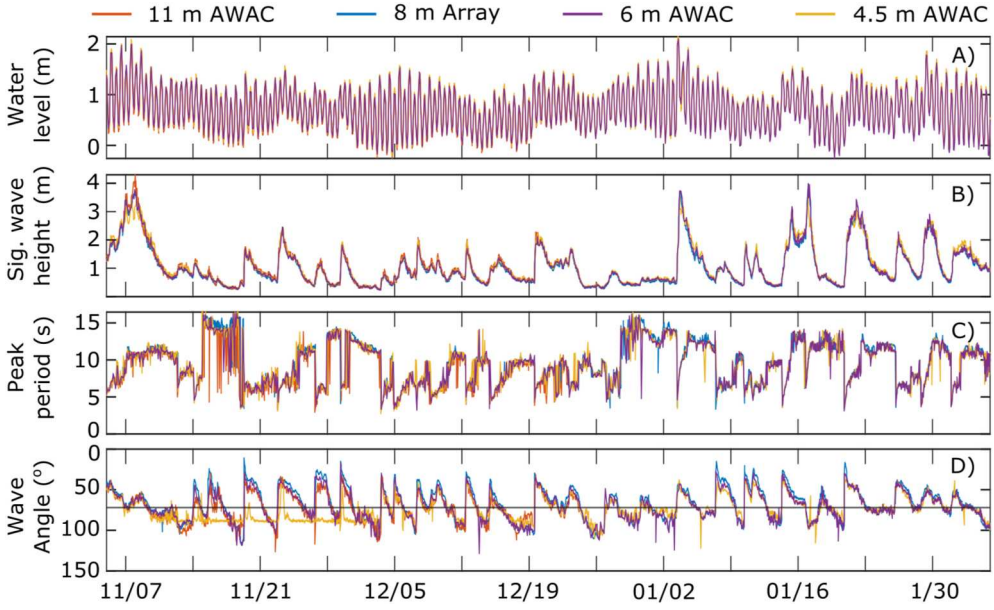

Fig. 3. Overview of nearshore conditions throughout the DAS deployment as measured by four seabed instruments (see Fig. 2 for instrument locations). A) Water level, B) significant wave height, C) peak period, and D) dominant wave angle with a black line showing the shore normal direction.

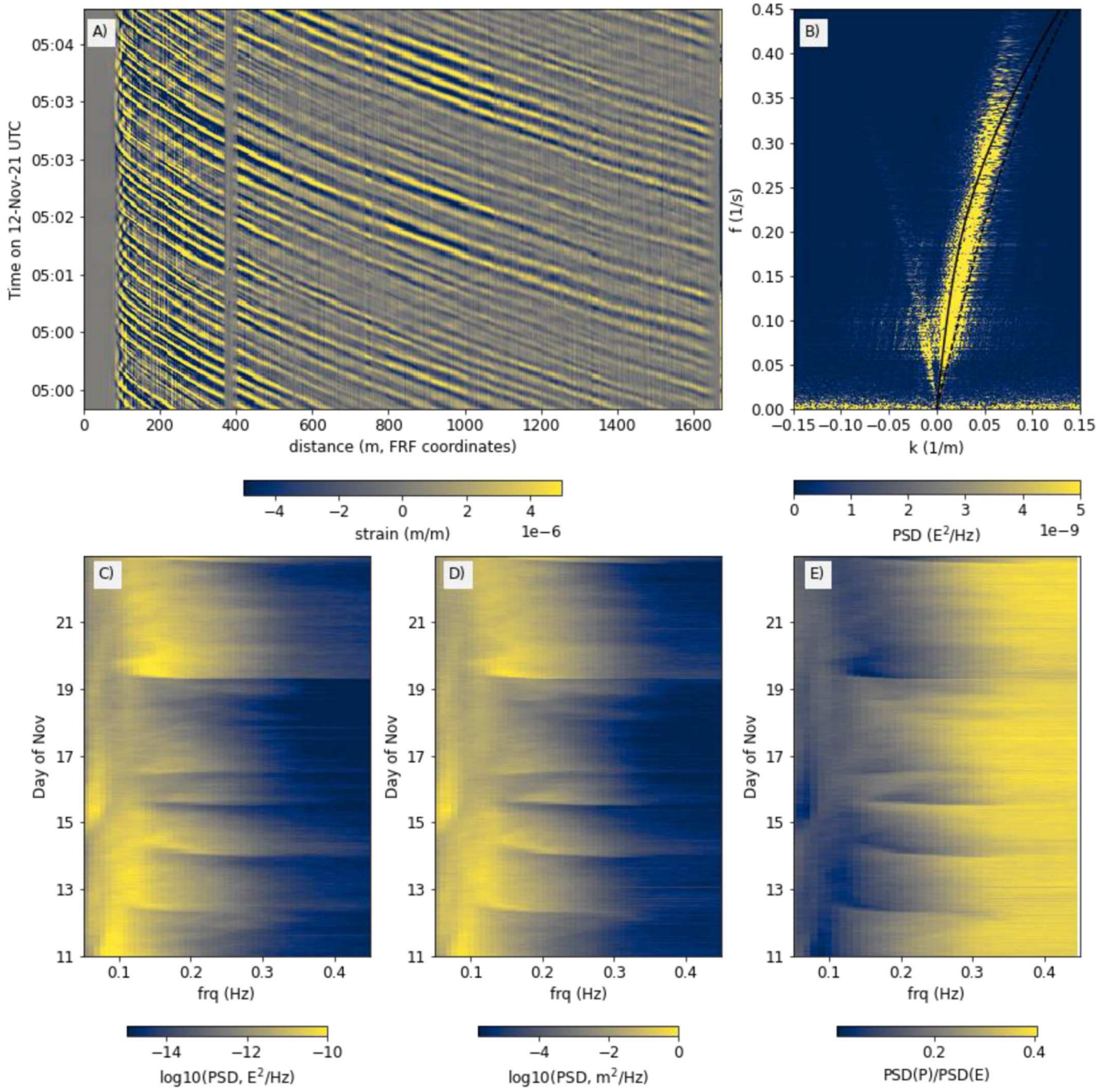

Fig. 4. Examples of raw DAS and pressure data. A) Time stack of strain for 5 min on November 12th. Waves appear as propagating bands of compression and extension. Optical fading appears as vertical lines of consistently low strain. B) frequency-wavenumber PSD from channels 70–540 for the 30-min window starting at 0-500 on November 12th. The theoretical dispersion curve for 10 m (solid line) and 2 m (dashed line) water depths are included for reference. C) Time stack of strain spectra at channel 436 every 30 min from November 11–23. D) Time stack of pressure spectra at the 11-m AWAC every 30 min from November 11–23. E) Time stack of the ratio between the spectra shown in C and D, demonstrating the frequency dependence of the strain-pressure relationship.

the energy weighted average period, the R^2 and rmse are 0.74–0.90 and 0.51–1.2 s, respectively, while for peak period estimates, the R^2 and rmse are 0.75–0.81 and 0.78–1.8 s, respectively. These values include time periods when the AWACs exhibit inconsistent wave-period estimates (e.g., Figs. 3C and 15–20 November). There are differences between the AWAC wave statistics calculated using the PUV method and the pressure alone (Table 1), with R^2 values of 0.58 for energy-weighted average period, 0.88 for peak period, and 0.9 for significant wave height. The accuracy of the DAS-derived wave statistics is constant over a wide range of dynamic conditions. The DAS and AWAC pressure records produced the least similar wave statistics during storm events, when DAS tended to estimate a shorter peak period than the AWACs. Overall, using the proposed calibration technique tended to underpredict the smallest measured significant wave heights and overpredict the largest measured significant wave heights (Fig. 6A, Fig. S5). The fit between calculated significant wave height and energy-weighted average period from the DAS and AWACs did not vary consistently with wave angle to shore (Fig. 6 A–B).

Variability in predicted wave height between adjacent DAS channels was typically ≪5 cm, especially offshore of the bar (Fig. 7). However,

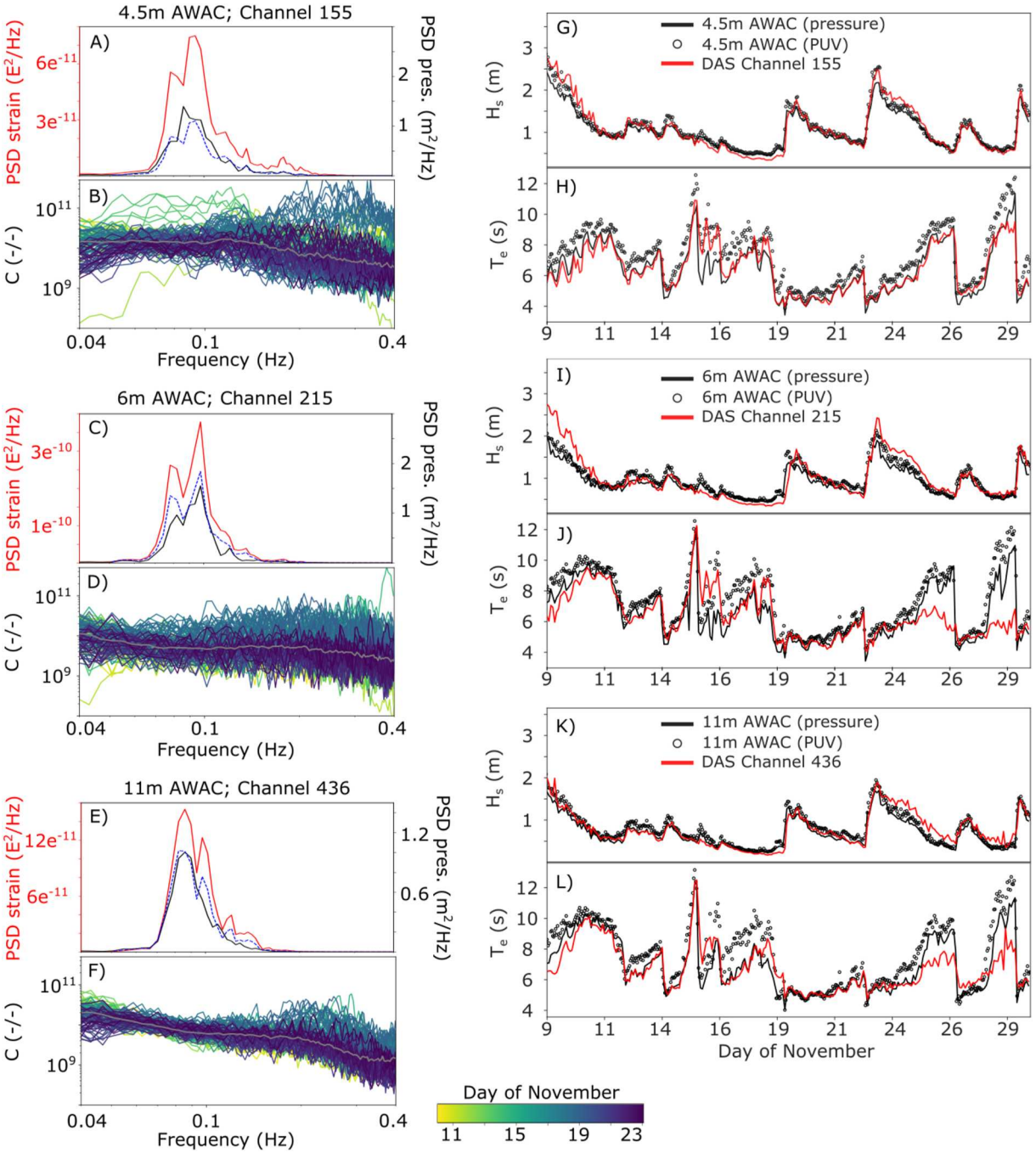

Fig. 5. Example calibration procedure and results for the three channels nearest to the AWACs (Channel 155 and 4.5-m AWAC; Channel 215 and 6-m AWAC; Channel 436 and 11-m AWAC) for November 2021. A-F) Example procedures for calculating a single correction factor and the median correction factor. The spectra of strain (red), pressure (black), and strain-derived pressure (dashed blue) on November 11, 2021 at 0400, with ~14 d. o.f., and the correction factors colored by date with the median in gray. G-L) The calculated significant wave height and energy-weighted average period from the strain-derived pressure, AWAC pressure alone, and AWAC PUV method (used by the FRF for published wave statistics).

Table 1
Comparison of the performance of DAS and AWAC methods for calculating significant wave height and energy weighted average period through November 2021. Range of rmse (m or s) values between the AWAC-pressure method and the nearest 3 DAS channels and between the AWAC-pressure and AWAC-PUV methods.

	DAS vs AWAC-P (11 m)	AWAC-PUV vs AWAC-P (11 m)	DAS vs AWAC-P (6 m)	AWAC-PUV vs AWAC-P (6 m)	DAS vs AWAC-P (4.5 m)	AWAC-PUV vs AWAC-P (4.5 m)
H_s (m)	0.2–0.21	0.12	0.19–0.21	0.19	0.13–0.63	0.11
T_e (s)	0.7–1.3	0.60	1.3–1.4	0.60	1.0–1.1	0.63

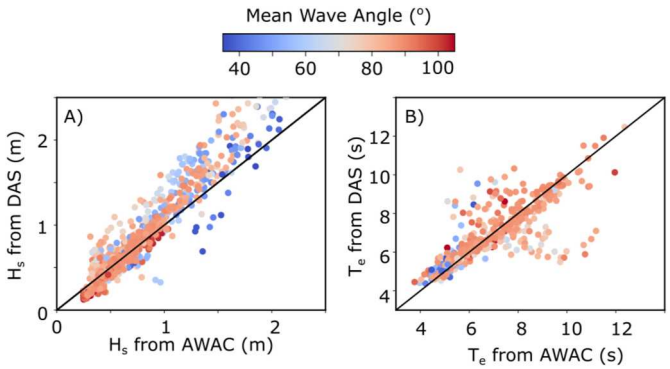

Fig. 6. One to one comparison of estimated significant wave height (A) and energy-weighted average period (B) for AWAC vs DAS derived statistics for the three channels nearest to the AWACs (Channel 155 and 4.5-m AWAC; Channel 215 and 6-m AWAC; Channel 436 and 11-m AWAC) in November 2021. Points are colored by the mean wave angle. The 1:1 line is included in black.

there were times when groups of DAS channels significantly underestimated the significant wave height (Fig. 7A and B). The channel-channel variability increased during time periods when the wave field was more three-dimensional. During these same time periods, the ratio of strain to pressure was also more variable (Fig. S6). The cross-shore trend in wave height was consistent between the DAS and the AWACs. The significant wave height immediately offshore of the bar was consistent with prediction of shoaling by linear wave theory (Fig. 7C). Inshore of the bar, the calculated wave height varied significantly from channel to channel.

The median correction factor varies spatially along the cable (Fig. 8); however, the shape of the calibration is consistent with the three examples shown in Fig. 5. The magnitude and shape of the correction factor does not vary consistently with distance from the nearest AWAC. The average R^2 and rmse values calculated using cross-validation at each channel for each month also vary spatially along the cable (Fig. 8). The channels nearest the AWACs have an average rmse of 0.13–0.63 m for significant wave height and 0.77–1.4 s for periods, with the poorest correlations occurring during the extremes of wave conditions. Channels periodically located in the swash zone are not consistent with the AWAC-derived wave statistics in deeper water, with $R^2 < 0.5$ and rmse values up to 1 m and 2–3 s. For December and January, the average accuracy is low at channels offshore of the kink, with most channels averaging $R^2 < 0.5$ (Fig. S7).

Calibration scenarios with limited validation data were evaluated to consider the influence of location of the AWAC with respect to DAS channel used for calibration. DAS strain was empirically calibrated to pressure at each channel using only one of the three AWACs. Calibrating using either the 11-m or 6-m AWACs results in performance comparable to the calibration generated using the nearest AWAC (Fig. 8). Across all

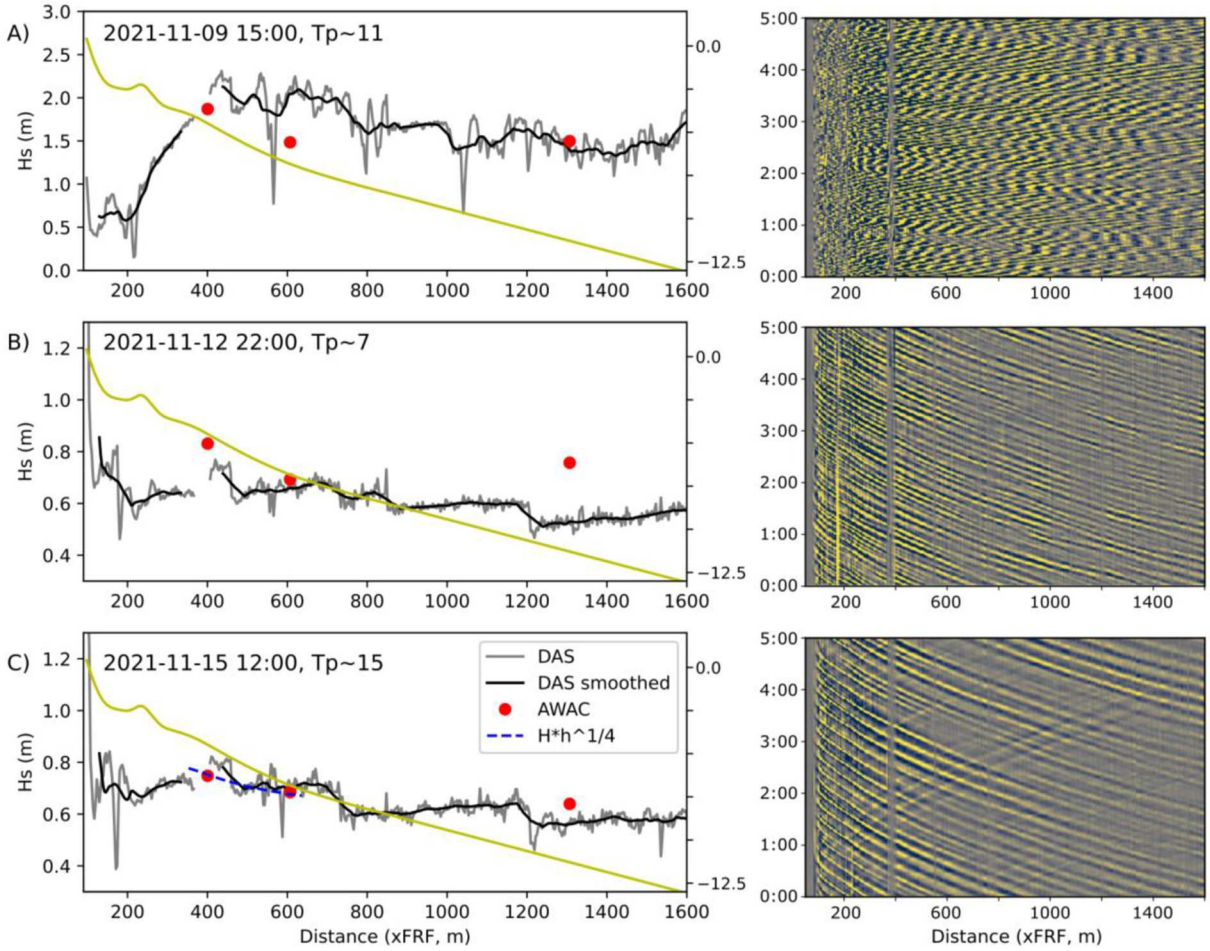

Fig. 7. Cross-shore significant wave height, calculated from each DAS channel at three time points with different wave heights and periods. The cross-shore profile of H_s is in gray with a boxcar smoothed line in black, and the three AWACs are shown as red points. Representative time-stacks of strain from the first 5 min of each period are included for reference. Note the change in y-axis scale in panel A). Theoretical shoaling from linear wave theory (blue line) is shown for the final panel, when the dominant period waves enter shallow water at ~6 m. Bathymetry from 17 November (yellow line) is included for reference. Data from the region of the kink have been removed.

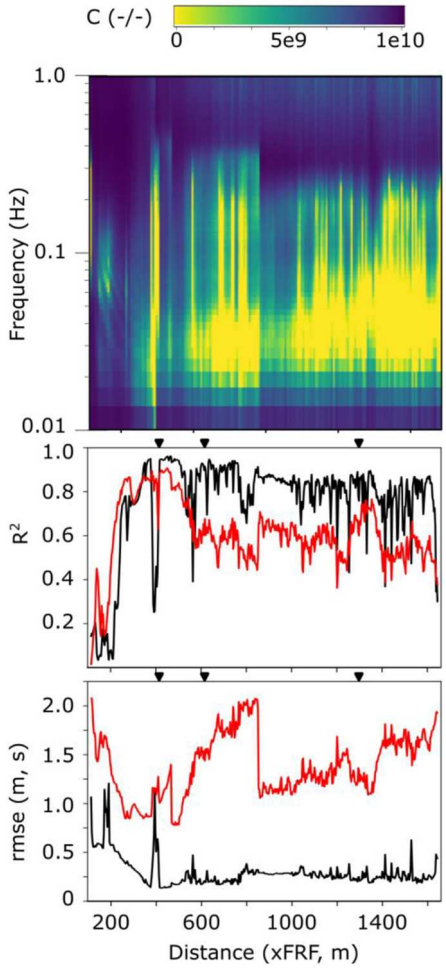

Fig. 8. Spatial variability in the empirical correction factor and the average, wave-parameter accuracy for November 2021 (see Fig. S7 for December and January). A) The median correction factor for each channel. B) The monthly averaged R^2 for the energy-weighted average period (red lines) and significant wave height (black lines). C) The monthly averaged rmse for the energy-weighted average period (red lines) and significant wave height (black lines). The AWAC locations are shown with black triangles.

unfaded channels, the median R^2 is 0.82 and 0.65 and rmse is 0.34 m and 1.6 s for significant wave height and energy-weighted average period, respectively. There is no clear trend in performance with distance from the calibration point using either of the deeper moorings. The performance decreases when only raw, un-shoaled data from the 4.5-m AWAC is used, with an average R^2 of 0.78 and 0.37 and rmse of 0.77 m and 2.7 s for significant wave height and energy-weighted average period, respectively.

The impact of calibration duration was also evaluated (Fig. 9). Initially, DAS is not well calibrated for wave height. Using only one day of calibration data to calculate a correction factor results in poor wave predictions of wave height from the DAS with R^2 as low as 0.32 and rmse of 6.2 m. The accuracy rapidly increases with increased calibration time, reaching maximal values between 10 and 15 days, depending on the channel. The accuracy of the energy-weighted average period is consistently >0.7 with any amount of calibration. Peak period is calculated accurately without calibration data, with a constant $R^2 >$ 0.75. The impact of time elapsed since calibration was assessed by evaluating the accuracy of wave parameters calculated in February using a November calibration. Channels inshore of xFRF~400 m have an average R^2 of 0.80 and 0.77 and rmse of 0.22 m and 1.6 s for significant wave height and energy-weighted average period, respectively.

4.3. Applications of DAS-derived pressure

The DAS-derived pressure at each channel records waves propagating onshore and shoaling (Fig. 10), much like the strain (Fig. 4). The frequency content of the derived pressure is consistent with the frequency content captured with the Argus camera array (Fig. 10C). The frequency content of the strain is remarkably consistent with the pressure over the incident band (Fig. 4C and D). This DAS-derived array of pressure also captures the evolution of waves as they interact with the shoreline. The cross-shore array revealed non-linear wave evolution over the sand bar (Fig. 11). Secondary waves were generated over the sandbar, which propagated onshore at a slower speed than the primary waves (Fig. 11B).

The DAS-derived pressure was also used to calculate wave reflection coefficients, centered at each channel, for the incident wave band (Fig. 12). The two DAS methods showed the same temporal and spatial trends with different magnitudes (Fig. 12A). The AWACs consistently provided higher estimates of reflection, and the coefficients calculated from the 4.5 m AWAC were anomalously high (>1). There was low correlation between the three methods for calculating wave reflection (Figs. S8–9). Reflection coefficients calculated using the RT method were generally <0.4 In the region approaching and over the sandbar, the wave reflection varied tidally and increased slightly with longer wave periods (Fig. 12B). Inshore of the sandbar, the wave reflection increased up to a maximum of 0.5, with greater variability between channels.

The DAS-derived pressure was used as an input for the cBathy algorithm, and the resulting bathymetry was compared against an interpolated cross-section from the most recent LARC survey (Fig. 13). cBathy is based on wave speeds, so any errors in calibration magnitude should have little effect. During the experiment, the nearshore bathymetric slope remained constant, and the sandbar migrated onshore over the study period (Fig. 2B). Creating a replicate 2D grid of DAS pressure is most accurate to the LARC survey in water depths <10 m with an average rmse of 0.64 m and 95% confidence interval of 0.14 m. The predicted bathymetry is least accurate in water >10 m and least precise, with an average rmse of 2.9 m and 95% confidence interval of 0.42 m (Fig. S10). The water depth is overpredicted in deeper waters. Using the 1-D version of cBathy results in slightly more accurate predictions of bathymetry with less precision. The average rmse to the LARC survey is 0.93 m and the average 95% confidence interval is 0.94 m. For the 1-D method, the water depth is underpredicted in both the shallowest and deepest regions and is overpredicted in the region between xFRF = 600–800 m. With both methods, the slope of the foreshore is well captured. Much of the misfit between DAS-derived bathymetry and the LARC survey appears as 10-m-scale oscillations (Fig. 13G). For an example comparison time on 17-Nov, the Argus cBathy output along the cable transect has an average rmse of 0.45 m and 95% confidence interval of 0.29 m out to ~450 m from the shoreline (~6 m water depths) and does not provide a depth estimate farther offshore.

5. Discussion

5.1. Empirical calibration of DAS strain to dynamic pressure

The primary goal of this study is to validate an empirical transfer function for converting Distributed Acoustic Sensing (DAS) strain to pressure at the seabed. A frequency-dependent coefficient was calculated from spectra of strain and *in-situ* pressure at three locations (Fig. 5), and the DAS-derived dynamic pressure (Fig. 10) was used to calculate bulk wave statistics. This simple and computationally efficient calibration method provided robust results (Fig. 5), demonstrating for the first time that DAS can be used to quantitatively measure nearshore wave heights and periods. The error between the DAS and AWAC-PUV outputs was comparable to the error between the AWAC-PUV and AWAC-pressure methods (Table 1), demonstrating the relative robustness of this DAS calibration method and the challenges of accurately measuring

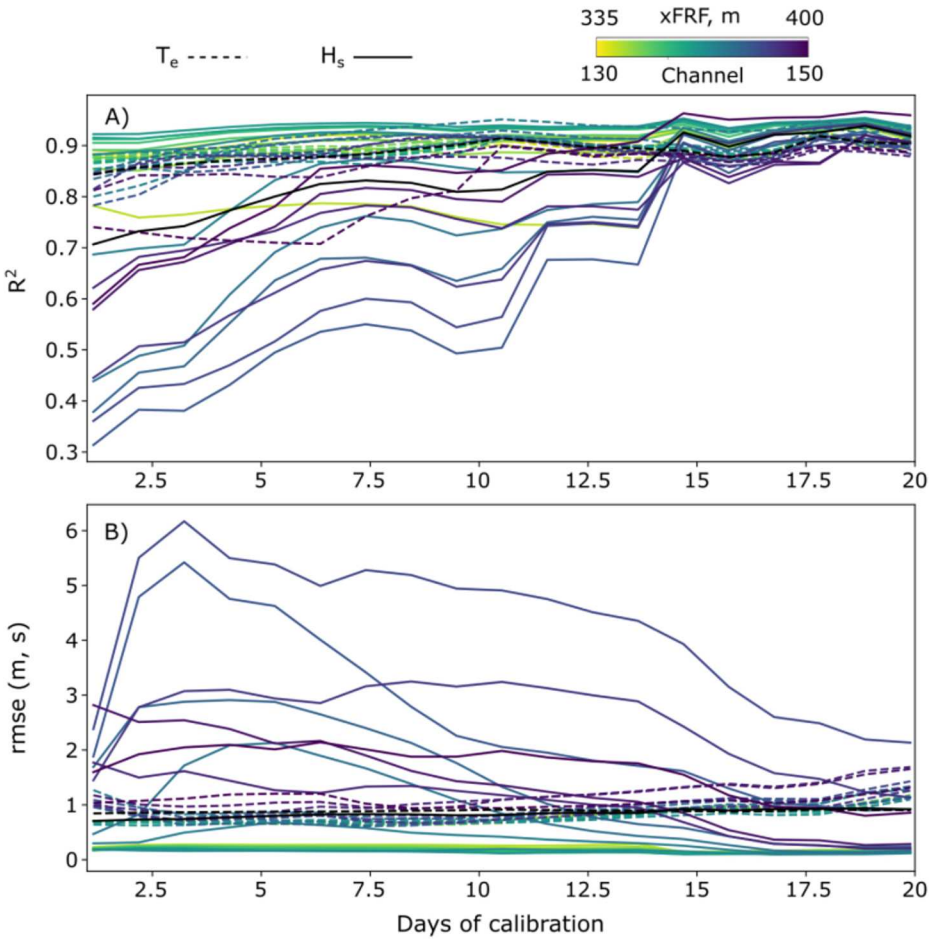

Fig. 9. Impact of calibration duration on accuracy of calculated wave parameters for channels inshore of channel 150, xFRF~400. A) The R^2 for the energy-weighted average period (dashed lines) and significant wave height (solid lines) for each calibration length between 1 and 20 days. B) The rmse for the period (dashed lines) and significant wave height (solid lines) for each calibration length between 1 and 20 days.

nearshore wave conditions. Calculations of wave statistics can be impacted by 3D wave fields, breaking waves, and sources of instrument noise (e.g., bubbles). It is worth noting that the AWAC can have its own known issues with estimating accurate wave period; the reported statistics do not reflect this observation and are purely comparing the AWAC derived estimate with the DAS derived estimate. The DAS-derived wave measurements were calculated during extremely calm and extremely energetic or stormy periods, which can create issues for camera imagery and radar (Holman and Haller, 2013). This type of real-time and continuous data could provide significant support to the development of offshore wind and wave-energy converters that are already connected to shore via fiber-optic cables. And, telecommunication cables and other existing cabled array networks could be leveraged to provide arrays of wave statistics with a single, onshore instrument.

Using a median correction factor for the empirical calibration did result in imperfect calculations of the extremes of wave conditions. The DAS spectral peaks were slightly high for the highest energy conditions and slightly low for the lowest energy conditions, leading to errors in the calculation of significant wave height (Fig. 6, Fig. S5). Variability in the correction factor estimated at any given wave condition is not only due to inherent measurement variability of DAS (i.e., fading), but also due to the 2D vs 3D nature of the wave field (Fig. S6). The median correction factor performed poorly during times when the wave field was chaotic and spatially variable (Fig. S6), likely related to differences between the actual spectral content recorded at the AWAC and at the DAS channel. Calibration and validation remain challenging issues. The method used here works well for the DAS locations closest to ground truth sensors, but optimal calibration would account for shoaling transformation. The 4.5 m AWAC does not provide a good validation point for channels located in the surf zone, and R^2/rmse values were worse in this region, as expected (Fig. 8). An optimal, though computationally expensive solution would be to calibrate against numerical models of the shoaling waves, seeded at ground truth points, or to develop machine learning models to relate pressure to strain, which may be better at capturing deviations at the extremes.

Calculations of wave height at adjacent DAS channels were most consistent offshore of the sandbar, and the performance was more variable between adjacent channels near the shoreline (Fig. 7). This variability may be related to changes in cable burial and coupling over the course of the deployment and optical fading, in addition to wave shoaling and breaking. Cable coupling to the seafloor is fundamentally related to the recorded strain (Reinsch et al., 2017; Ugalde et al., 2022; Williams et al., 2022), making the use of a single empirical correction factor for the whole month less accurate. Additionally, in the shallowest water depths, DAS may be measuring strain signals related to more than just water surface deviation (e.g., wave breaking impact, bed shear stress). Overall, collecting a cross-shore array of observations with DAS produces substantially more datapoints, providing the ability to cross-check and remove measurements with high uncertainty.

The dataset presented here was collected at the USACE FRF, where there are multiple, continuously operated systems for recording waves. However, this volume of pressure calibration data will not always be available, and the impact of limited spatial and temporal calibration was

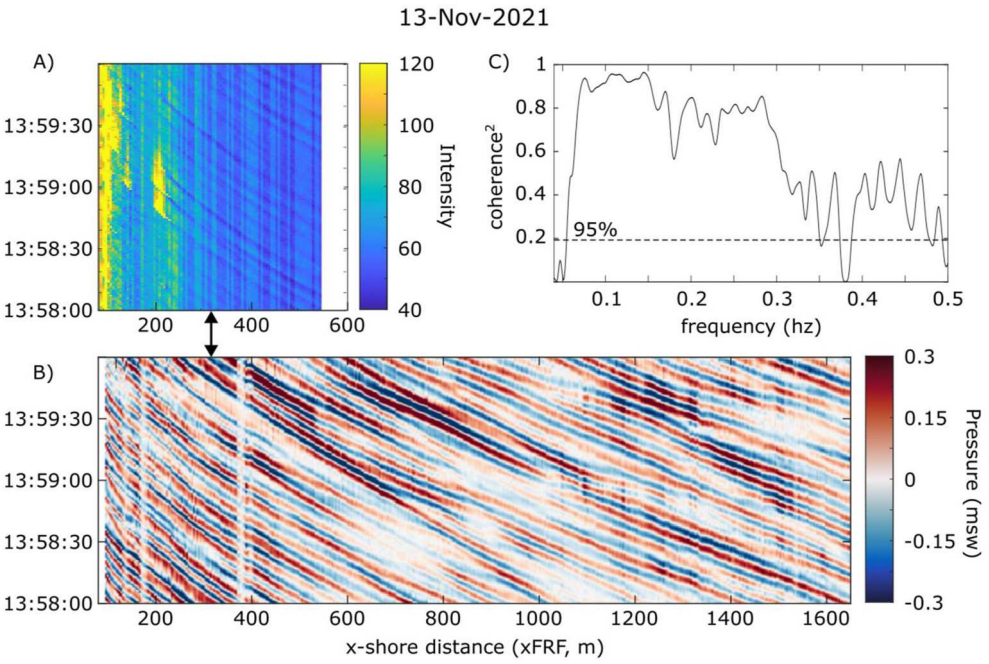

Fig. 10. Comparison of Argus time-stack and DAS-derived pressure on November 13, 2021 for 120 s. A) Time stack of pixel intensity from the Argus cameras. B) DAS-derived pressure at channels 56–550. Note that the sign of pressure may be incorrect, as the phase relationship between pressure and strain has not been validated. C) Coherence of spectra calculated from Argus intensity and DAS pressure at cross-shore location 325 (shown with an arrow) with 30 d. o.f.

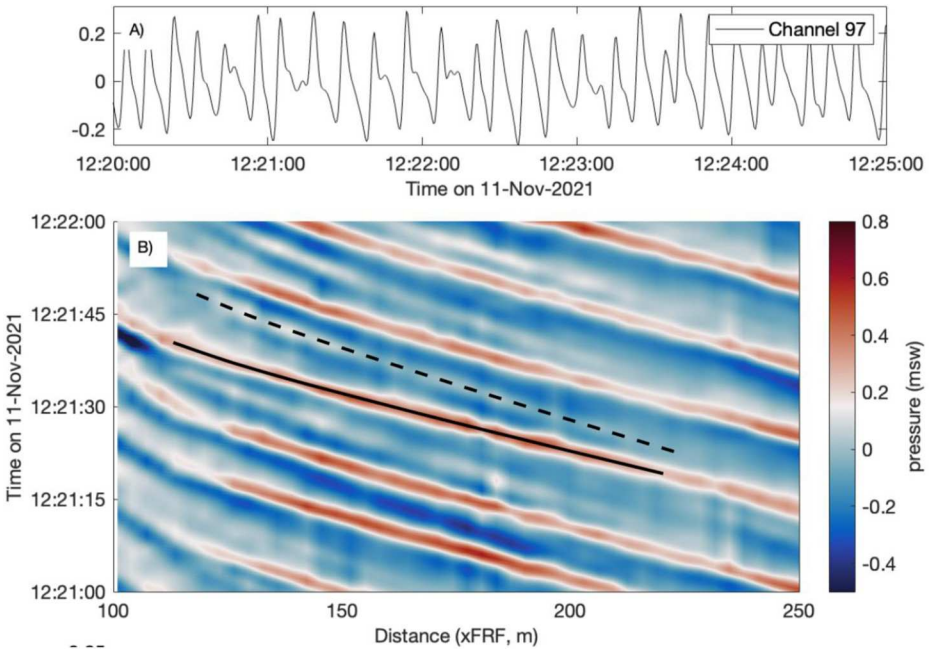

Fig. 11. Wave evolution over the sand bar. A) Time series of pressure derived at channel 97. B) Time stack of pressure at the channels between the bar and the swash zone, highlighting secondary waves generated over the bar (crest is near xFRF = 243 m). The primary wave crest is highlighted with a solid line and the secondary crest is highlighted with a dashed line. Note that the wave phase or sign of pressure may be incorrect, as the phase relationship between pressure and strain has not been validated.

considered. Using only one calibration sensor moderately reduced the accuracy of the DAS-derived wave parameters for locations offshore of the sandbar. Using only the AWAC nearest the sandbar resulted in a poor calibration (Fig. 8), which was likely related to wave shoaling as well as the attenuation of higher-frequency pressure signals with depth. As expected, the shape of the pressure spectra in 4 m of water was not representative of the strain spectra in 11 m of water.

Varying the timing and length of the calibration also demonstrated the importance of considering low-frequency and monthly signals. The magnitude of the signal recorded on the cable changed as the cable self-buried over the course of a week (Fig. S3). This increase in recorded strain is consistent with previous studies of cable coupling and strain resolution (Ide et al., 2021; Lior et al., 2021; Matsumoto et al., 2021; Ugalde et al., 2022; Vantassel et al., 2022). Optimal calibration was achieved after burial (Fig. S4). In the post-burial period, 10–15 days of calibration were required to calculate a representative conversion factor

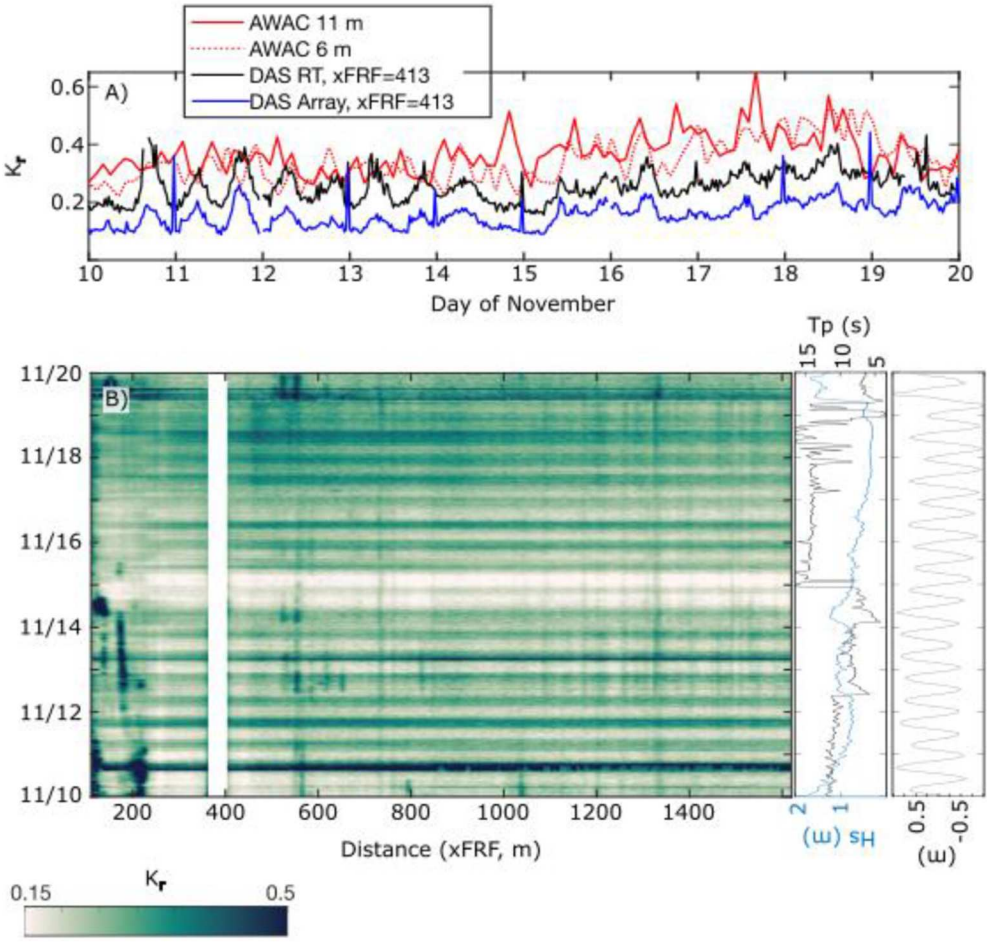

Fig. 12. Wave reflection coefficient, K_r, calculated from DAS using the Radon Transform (RT) and array methods and from the AWACs using pressure and velocity. A) DAS K_r calculated every 30 min at xFRF = 413 and at the 6 and 11 m AWACs. B) DAS K_r from the RT method calculated every 30 min from 10 to 20 November 2021. The tidal stage, significant wave height, and peak period at the 11-m AWAC are shown for reference.

for the more frequency-sensitive parameters of significant wave height and energy-weighted average period (Fig. 9). The length of this calibration period may be related to optical interferometric uncertainty in gauge length and location. Peak period was accurately captured by DAS strain with no calibration. The accuracy of wave statistics calculated using a single correction factor from the beginning of the deployment did decrease even for channels unaffected by the kink, suggesting that long-term changes in cable burial or coupling can impact the calibration. Future investigations of the low-frequency signals could provide a stronger understanding of the fundamental physical processes underlying this temporal variability in the calibration. Specifically, changes in the frequency content of the strain signals may be related to changes in cable temperature (Sidenko et al., 2022) and cable burial. Targeted, long-term experiments with DAS could provide insight into the parameters necessary for ongoing calibration, as have been developed for photogrammetry or acoustic instrumentation.

The physical shape of the frequency-dependent correction factor, C, (Eqn. (2)) could be explained by analytically accounting for the mechanisms generating stress on the cable and calculating transferred cable strain from that stress, a subject of ongoing work. Shallow-water ocean waves generate a seafloor pressure gradient (Fig. 1, Eqn. (1)) as well as bed shear stress. Cable stress is also generated by seafloor compliance, which may dominate the strain signal in some cases, as well as microseism in other cases (Mecozzi et al., 2021; Taweesintananon et al., 2023; Williams et al., 2022). Here, these stresses as well as the stress-strain transfer function are encompassed by the frequency-dependent correction factor. Consequently, seismologic studies of seafloor compliance from DAS and ocean waves may require a fundamentally different methodology. Fully accounting for these variables would require knowing the modulus of elasticity of the cable, the coupling or strain-transfer efficiency of each cable component, the composition of the seabed, the depth of burial, and the properties of the transmitted laser pulse (Hubbard et al., 2022; Sidenko et al., 2022; Taweesintananon et al., 2021; Vantassel et al., 2022). All of these variables may not be known *a priori* for all points along a cable, especially for commercial telecommunication cables installed on the continental shelf. The empirical calibration method presented here may be the most logistically realistic method for many oceanographic DAS applications. It is also important to note that wave angle did not significantly impact the calculation of wave parameters in this study (Fig. 6). However, the integrated strain recorded by DAS will decrease sinusoidally with increasing wave angle, and it is likely that this experiment did not record waves with a large enough angle to the cable to result in this signal loss. Future experiments should account for signal loss if the wave angle to the cable exceeds 45°.

Overall, the methodology for transferring DAS-measured strain to dynamic pressure and the validation of DAS-derived dynamic pressure of propagating shallow and intermediate water depth waves is a major contribution of this study. The calibration method here is specifically tailored towards capturing the near-bed dynamic pressure under shallow-water waves, where dynamic pressure is the dominant strain source. The pressure and strain records in this dataset were not time-synched to sub-minute accuracy and cannot be used to directly compare phase-resolved pressure between methods of measurement.

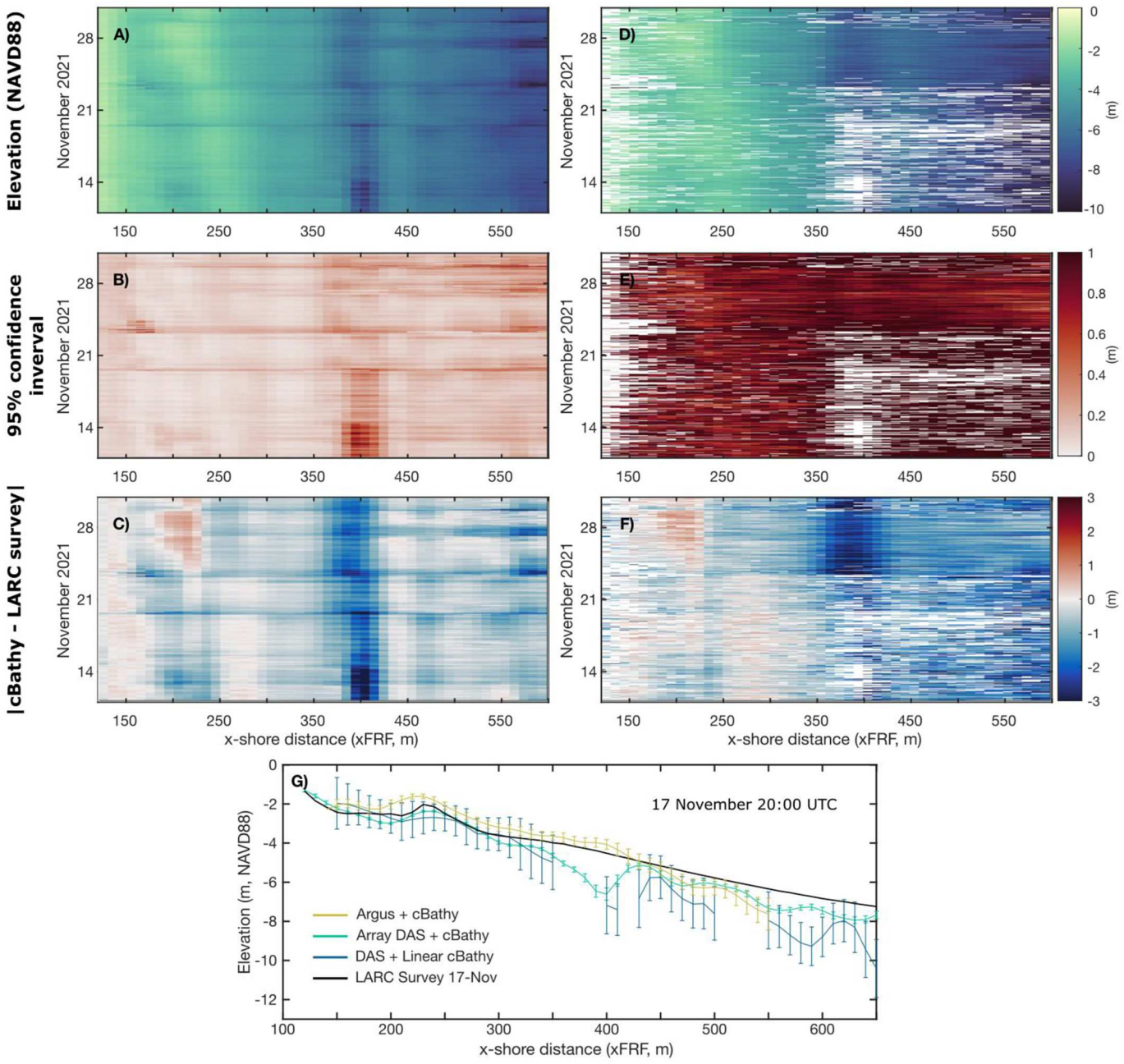

Fig. 13. Result of applying DAS-derived pressure to the cBathy algorithm using A-C) replicated DAS data and D-F) the linearized 1-D version of cBathy. The top row shows the bathymetric output, the second row shows the 95% confidence interval calculated after the Kalman filter, and the third row shows the difference between the calculated bathymetry and the nearest LARC survey. G) The cross-shore bathymetry around the sandbar from the DAS cBathy methods, Argus camera imagery and cBathy, and the LARC survey on November 17, 2021 at 20:00 UTC. The full cross-shore profiles, to xFRF~1500 m, are included in Supporting Information (Fig. S10).

However, the success of the calibration suggests that DAS strain can record the dynamic pressure of individual waves propagating over a gauge length (Fig. 10), as long as the gauge length is set short enough to generate multiple strain measurements within a wavelength. This method would not be physically appropriate for recording deep-water waves. Previous applications of DAS to observe surface waves have primarily utilized the strain generated by microseism associated with wave-wave interactions in deeper water (Viens et al., 2022; Williams et al., 2019, 2022). The empirical calibration developed here, as well as the calibration method, can be tested at more field sites. New field experiments should also examine the deep-water boundaries of this type of dynamic-pressure-based calibration.

5.2. Using DAS-derived measurements to explore a cornucopia of nearshore processes

The DAS provides measurements of wave parameters throughout the nearshore (Figs. 7 and 9), which is logistically challenging and prohibitively expensive with point sensors. Understanding the nearshore sources and sinks for incident-band wave energy is fundamental for predicting nearshore processes and beach evolution. The dense, cross-shore array of DAS data was used to explore some of these processes (Fig. 7). It is important to note for these analyses that the phase relationship between DAS strain and pressure has not been resolved and that DAS has not been tested against co-located and time-synched surf-zone

instrumentation. Despite these considerations, the data show some interesting features.

During moderate wave conditions (H_s = 0.74 m, T_p = 11 s), it appears that secondary waves were generated over the sandbar (Fig. 11). This generation of secondary, harmonic waves over a sand bar under moderate wave conditions has long been observed in laboratory and field studies (Beji and Battjes, 1993; Byrne, 1969; Elgar et al., 1997; Norheim et al., 1998). Non-linear wave transformation has important consequences for wave reflection and dissipation (Masselink, 1998), and models that apply a frequency-integrated or bulk energy dissipation coefficient will not capture this evolution. The range of wave conditions that promote the release of harmonics over a bar are not fully defined, and the importance of collecting better measurements of non-linear wave evolution has been highlighted (Martins et al., 2020; Saprykina and Kuznetsov, 2022; Senechal et al., 2002). DAS-derived cross-shore profiles of pressure, coupled with traditional point measurements, could provide new insights into wave-shape evolution across the surf zone, especially with future advances in our understanding of the relationships between DAS strain and hydrodynamic signals.

DAS-derived pressure was also used to calculate incident-band wave reflection (Fig. 12). Generally, cross-shore field measurements of wave reflection coefficients are limited by the logistical feasibility of installing pressure sensors or lidar arrays (Martins et al., 2017b), with many calculation methods based on the use of 3–4 sensors (Baquerizo et al., 1997, 1998; Lin and Huang, 2004; Zelt and Skjelbreia, 1992). In the region offshore of the sandbar, the overlapping arrays of DAS channels produced consistent estimates of wave reflection with 95% confidence intervals <0.1, indicating that any single array would accurately represent this region. The ratio of reflected energy was generally 0.2–0.4, consistent with value expected for a natural, sandy beach and increased during times with longer wave periods and greater wave heights as predicted by theory (Ardhuin and Roland, 2012; Elgar et al., 1994). Inshore of the sandbar, the reflection coefficients were greater overall and estimates between locations were more variable.

The calculations of wave reflection demonstrate the combined power of the DAS array and the Radon Transform separation method, which can utilize a dense data array (Almar et al., 2014). Visually, it appears that the RT method outperforms the array method in separating incoming versus outgoing waves (Figs. S7–8). Consequently, the reflection coefficients calculated using the RT method were less variable between adjacent channels. The two methods produced consistently different estimates of reflection, and both estimates derived from DAS were lower than the reflection coefficients calculated from the AWAC pressure and velocity. This difference is consistent with previous comparisons between array and single-point methods in the infragravity band (de Bakker et al., 2014), indicating that comparisons between the AWAC and DAS array methods may not be valid for evaluation.

Overall, the cross-shore DAS data demonstrate the challenges of accurately capturing wave energy flux in this complex region using just one array of sensors. The increase in reflection over the bar and up to 0.5 near the shoreline is consistent with theory and previous field experiments (Almar et al., 2019; Baquerizo et al., 1997; Martins et al., 2017a). Models accounting for both bathymetric and shoreline sources of reflection will be better able to capture this cross-shore variability (Zhang et al., 2021), instead of applying a single offshore coefficient.

The continuous DAS record also captured variability in reflection through a range of wave conditions, especially at the sandbar (Fig. 12B). Wave reflection was greatest during times with longer period waves and high tide, consistent with previous observations of wave reflection correlating positively with bathymetric slope and offshore wave period (Almar et al., 2018; Battjes, 1974; Gomes da Silva et al., 2019; Martins et al., 2017a). However, the role of tidal stage has been challenging to capture since many of these field experiments are designed to only collect data at high tide. Tidal stage may impact wave reflection both through water depth and the presence of currents, which can diffract waves (Ardhuin et al., 2012; Hauser et al., 2023). DAS techniques provide a promising opportunity to explore the relationships between wave reflection, dissipation, runup, and tidal stage. The continuous DAS data stream could also be used to examine cross-shore changes in infragravity wave reflection, which can strongly impact runup (Bertin et al., 2020; De Bakker et al., 2014; Inch et al., 2017b; Melito et al., 2022; Sheremet et al., 2002, 2014; Thomson et al., 2006). The investigation of infragravity wave reflection from DAS would also require specific validation, as we only focus on incident-band waves here.

The bathymetry derived from DAS and cBathy captured the slope of the nearshore region and the location of the sandbar (Fig. 13). cBathy relies on wave phase speed to determine depth, normalizing the spectral magnitude. The successful use of DAS with cBathy suggests that DAS can accurately track the progression of wave even in the absence of good calibrations. Both the nearshore slope and cross-shore sandbar locations are important parameters for predicting beach stability, runup, and wave reflection (Almar et al., 2019; Battjes, 1974; Gomes da Silva et al., 2020, 2019; Grossmann et al., 2023; Ruggiero et al., 2001b). However, a linear cable deployment does not capture along-shore variability, which can have a strong impact on beach processes especially rip current formation and evolution (Almar et al., 2018; Baker et al., 2021). Neither linear adaptation of cBathy resulted in bathymetric predictions with cm-scale precision or accuracy. This sub-meter-scale accuracy is challenging to obtain with any remote method, and cBathy derived from Argus camera imagery has a rmse of 0.38 m at the FRF (Holman and Bergsma, 2021) and up to 2.05 m at other sites (Brodie et al., 2018 and references therein).

Collecting measurements in the swash zone and nearshore is challenging, and DAS can serve as a multifaceted tool for monitoring multiple processes simultaneously. In this experiment, the shoreline position was identified to within a gauge length (Fig. S11, Text S1), and future experiments targeting the shoreline could use a smaller gauge length than that used here (3.2 m). The most compelling advantage of DAS is its spatial resolution and coverage (Fig. 10); it provides insight into the spatial variability of nearshore processes at the seabed without altering flow, which no other technology can provide at this time. Many nearshore signals were recorded within this dataset that are not explored here. Future applications of DAS could focus on acoustic signals from wave breaking, bedform migration, beach infiltration/exfiltration, infragravity waves and wave reflection. There are also opportunities for exploring interdisciplinary topics across physical oceanography and marine geophysics, such as the relationship between infragravity waves and seismic hum (Bromirski, 2002; Traer et al., 2012) or submarine landslide hazards at the shelf break (Spica et al., 2020, 2022).

6. Conclusions

Distributed fiber optic sensing is an emerging technology that provides a dense spatial array of measurements along a fiber optic cable. The goal of this work was to demonstrate, validate, provide methodology for, and explore a new method for measuring nearshore and foreshore processes using Distributed Acoustic Sensing measurements of fiber-optic cable strain. DAS data were collected continuously at 3.2 m spacing to ~1500 m offshore at the USACE FRF, where ground-truth data was provided by AWAC sensor packages in 4.5, 6 and 11 m mean depth. An empirical calibration from DAS strain to pressure was developed based on the frequency-dependent gain, $C(x,f)$. The DAS-derived pressure was used to calculate measurements of bulk wave statistics throughout the nearshore and foreshore, with typical rmse of 0.2 m for significant wave height and 1 s for energy-weighted average period for channels near the ground-truth. Of note, DAS comparisons were made with AWAC-derived significant wave height and energy containing period, which have their own inherent estimate uncertainty. Wave reflection was calculated from the array of DAS-derived pressure. This is the first field experiment to show that DAS data collection on telecommunication cables can be used to measure waves in the coastal zone. Measurements were successfully collected through a wide range of

dynamic conditions, including storm events. The calibration optimally required at least 1–2 pressure sensors deployed for 10–15 days. The success of this simple, empirical calibration suggests that DAS could be used to leverage existing cable array networks to monitor wave conditions.

Preliminary applications for this cross-shore array of near-bed data were also explored. The data were used to determine bathymetry with cBathy and approximate the shoreline position. DAS has the capability to monitor nearshore and foreshore processes simultaneously and non-intrusively, providing a promising new method for continuous sea-bed measurement. There are numerous possibilities for the expansion of oceanographic DAS techniques, and this study is not intended to be comprehensive. Future projects could also explore the integration of DAS strain with complimentary data streams from remote sensing and *in-situ* point sensors.

Many questions remain in understanding the full range of signals recorded by DAS strain. Future work should explore the strain signals induced by oceanographic temperature fluctuations, cable burial and bedform migration, and groundwater flow. Yet, these results show that fiber-optic methods provide a promising new opportunity for continuous, dense, spatially distributed oceanographic data collection in challenging coastal environments.

Data statement

The raw Distributed Acoustic Sensing data is hosted at Oregon State University and is available upon request. The decimated DAS data at 2 Hz is available via NHERI DesignSafe (https://doi.org/10.17603/ds2-89q3-5x76). Data supplied by the Field Research Facility is available for download directly through their website (https://frfdataportal.erdc.dren.mil/).

CRediT authorship contribution statement

H.E. Glover: Data curation, Formal analysis, Methodology, Software, Visualization, Writing – original draft. **M.E. Wengrove:** Conceptualization, Data curation, Funding acquisition, Investigation, Methodology, Project administration, Software, W. **R. Holman:** Methodology, Software, Writing – review & editing.

Declaration of competing interest

The authors declare that they have no known competing financial interests or personal relationships that could have appeared to influence the work reported in this paper.

Data availability

See Data Availability Statement

Acknowledgements

This work was funded by ONR Grants N00014-21-1-2676 and N00014-20-1-2591 and NAVFAC Grant N00024-21-D-6400. The authors thank CTEMPs, especially Cara Walter, funded by NSF EAR awards 1832109 and 1832170, for support in experimental design and equipment management. The authors thank the field technicians and scientists at the US Army Corps of Engineers Engineering Research and Development Center Field Research Facility for making the cable deployment possible and supplying additional data for our analysis. We would also like to thank Ryan Mieras for an illuminating conversation that sparked the idea to apply cBathy to DAS. Finally, we would like to thank Nate Lindsey, Marcela Ifju, the engineers at Sintela, and the scientists of the DAS NSF RCN for ongoing support with data analysis.

Appendix A. Supplementary data

Supplementary data to this article can be found online at https://doi.org/10.1016/j.coastaleng.2024.104487.

References

Almar, R., Blenkinsopp, C., Almeida, L.P., Catalán, P.A., Bergsma, E., Cienfuegos, R., Viet, N.T., 2019. A new remote predictor of wave reflection based on runup asymmetry. Estuar. Coast Shelf Sci. 217, 1–8. https://doi.org/10.1016/j.ecss.2018.10.018.

Almar, R., Michallet, H., Cienfuegos, R., Bonneton, P., Tissier, M., Ruessink, G., 2014. On the use of the Radon Transform in studying nearshore wave dynamics. Coast. Eng. 92, 24–30. https://doi.org/10.1016/j.coastaleng.2014.06.008.

Almar, R., Nicolae Lerma, A., Castelle, B., Scott, T., 2018. On the influence of reflection over a rhythmic swash zone on surf zone dynamics. Ocean Dynam. 68, 899–909. https://doi.org/10.1007/s10236-018-1165-5.

Almeida, L.P., Almar, R., Blenkinsopp, C., Senechal, N., Bergsma, E., Floc'h, F., Caulet, C., Biausque, M., Marchesiello, P., Grandjean, P., Ammann, J., Benshila, R., Thuan, D.H., da Silva, P.G., Viet, N.T., 2020. Lidar observations of the swash zone of a low-tide terraced tropical beach under variable wave conditions: the Nha Trang (Vietnam) COASTVAR experiment. J. Mar. Sci. Eng. 8 https://doi.org/10.3390/JMSE8050302.

Anderson, D., Bak, A.S., Cohn, N., Brodie, K.L., Johnson, B., Dickhudt, P., 2023. The impact of inherited morphology on sandbar migration during mild wave seasons. Geophys. Res. Lett. 50, 1–11. https://doi.org/10.1029/2022GL101219.

Ardhuin, F., Roland, A., 2012. Coastal wave reflection, directional spread, and seismoacoustic noise sources. J. Geophys. Res. Oceans 117. https://doi.org/10.1029/2011JC007832.

Ardhuin, F., Roland, A., Dumas, F., Bennis, A.C., Sentchev, A., Forget, P., Wolf, J., Girard, F., Osuna, P., Benoit, M., 2012. Numerical wave modeling in conditions with strong currents: dissipation, refraction, and relative wind. J. Phys. Oceanogr. 42, 2101–2120. https://doi.org/10.1175/JPO-D-11-0220.1.

Ardhuin, F., Stopa, J.E., Chapron, B., Collard, F., Husson, R., Jensen, R.E., Johannessen, J., Mouche, A., Passaro, M., Quartly, G.D., Swail, V., Young, I., 2019. Observing sea states. Front. Mar. Sci. 6, 1–29. https://doi.org/10.3389/fmars.2019.00124.

Baker, C.M., Moulton, M., Raubenheimer, B., Elgar, S., Kumar, N., 2021. Modeled three-dimensional currents and eddies on an alongshore-variable barred beach. J. Geophys. Res. Oceans 126. https://doi.org/10.1029/2020JC016899.

Baldock, T.E., Simmonds, D.J., 1999. Separation of incident and reflected waves over sloping bathymetry. Coast. Eng. 38 (3), 167–176.

Baquerizo, A., Losada, M.A., McKee Smith, J., Kobayashi, N., 1997. Cross-shore variation of wave reflection from beaches. J. Waterw. Port, Coast. Ocean Eng. 123, 274–279.

Baquerizo, A., Losada, M.A., Smith, J.M., Baquerizot, A., Losadat, M.A., Smiths, J.M., 1998. Wave reflection from beaches: a predictive model. J. Coast Res. 14 (1), 291–298.

Battjes, J.A., 1974. Surf similarity. In: Proceedings of the 14th Conference on Coastal Engineering, pp. 466–480. Copenhagen, Denmark.

Beji, S., Battjes, J.A., 1993. Experimental investigation of wave propagation over a bar. Coast. Eng. 19, 151–162.

Bell, P.S., 1999. Shallow water bathymetry derived from an analysis of X-band marine radar images of waves. Coast. Eng. 37, 512–527.

Bertin, X., Martins, K., de Bakker, A., Chataigner, T., Guérin, T., Coulombier, T., de Viron, O., 2020. Energy transfers and reflection of infragravity waves at a dissipative beach under storm waves. J. Geophys. Res. Oceans 125. https://doi.org/10.1029/2019JC015714.

Birkemeier, W.A., DeWall, A.E., Corbics, C.S., Miller, H.C., 1981. A User's Guide to CERC's Field Research Facility.

Boehm, A.B., Ismail, N.S., Sassoubre, L.M., Andruszkiewicz, E.A., 2017. Oceans in peril: grand challenges in applied water quality research for the 21st century. Environ. Eng. Sci. 34, 3–15. https://doi.org/10.1089/ees.2015.0252.

Bouffaut, L., Taweesintananon, K., Kriesell, H.J., Rørstadbotnen, R.A., Potter, J.R., Landrø, M., Johansen, S.E., Brenne, J.K., Haukanes, A., Schjelderup, O., Storvik, F., 2022. Eavesdropping at the speed of light: distributed acoustic sensing of baleen whales in the arctic. Front. Mar. Sci. 9 https://doi.org/10.3389/fmars.2022.901348.

Brodie, K.L., Dyer, T., Spore, N., Slocum, R., O'Dea, A., Whitesides, T., Alexander, R., 2017. Continuously Operating Dune-Mounted Lidar System at the Field Research Facility, A Report Detailing Lidar Collection, Processing, Evaluation, and Product Development.

Brodie, K.L., Palmsten, M.L., Hesser, T.J., Dickhudt, P.J., Raubenheimer, B., Ladner, H., Elgar, S., 2018. Evaluation of video-based linear depth inversion performance and applications using altimeters and hydrographic surveys in a wide range of environmental conditions. Coast. Eng. 136, 147–160. https://doi.org/10.1016/j.coastaleng.2018.01.003.

Brodie, K.L., Raubenheimer, B., Elgar, S., Slocum, R.K., McNinch, J.E., 2015. Lidar and pressure measurements of inner-surfzone waves and setup. J. Atmos. Ocean. Technol. 32, 1945–1959. https://doi.org/10.1175/JTECH-D-14-00222.1.

Bromirski, P.D., 2002. The near-coastal microseism spectrum: spatial and temporal wave climate relationships. J. Geophys. Res. 107 https://doi.org/10.1029/2001jb000265.

Buscombe, D., Rubin, D.M., Warrick, J.A., 2010. A universal approximation of grain size from images of noncohesive sediment. J. Geophys. Res. Earth Surf. 115, 1–17. https://doi.org/10.1029/2009jf001477.

Byrne, R.J., 1969. Field occurrences of induced multiple gravity waves. J. Geophys. Res. 74, 2590–2596. https://doi.org/10.1029/jb074i010p02590.
Carini, R.J., Chickadel, C.C., Jessup, A.T., 2021. Surf zone waves at the onset of breaking: 1. LIDAR and IR data fusion methods. J. Geophys. Res. Oceans 126, 1–18. https://doi.org/10.1029/2020JC016934.
Carini, R.J., Chickadel, C.C., Jessup, A.T., Thomson, J., 2015. Estimating wave energy dissipation in the surf zone using thermal infrared imagery. J. Geophys. Res. Oceans 120, 3937–3957. https://doi.org/10.1002/2014JC010561.
Chardón-Maldonado, P., Pintado-Patiño, J.C., Puleo, J.A., 2016a. Advances in swash-zone research: small-scale hydrodynamic and sediment transport processes. Coast. Eng. 115, 8–25. https://doi.org/10.1016/j.coastaleng.2015.10.008.
Chardón-Maldonado, P., Pintado-Patiño, J.C., Puleo, J.A., 2016b. Advances in swash-zone research: small-scale hydrodynamic and sediment transport processes. Coast. Eng. 115, 8–25. https://doi.org/10.1016/j.coastaleng.2015.10.008.
Dalrymple, R.A., MacMahan, J.H., Reniers, A.J.H.M., Nelko, V., 2011. Rip currents. Annu. Rev. Fluid Mech. 43, 551–581. https://doi.org/10.1146/annurev-fluid-122109-160733.
De Bakker, A.T.M., Tissier, M.F.S., Ruessink, B.G., 2014. Shoreline dissipation of infragravity waves. Continent. Shelf Res. 72, 73–82. https://doi.org/10.1016/j.csr.2013.11.013.
Elgar, S., Guza, R.T., Raubenheimer, B., Herbers, T.H.C., Gallagher, E.L., 1997. Spectral evolution of shoaling and breaking waves on a barred beach. J. Geophys. Res. Oceans 102, 15797–15805. https://doi.org/10.1029/97JC01010.
Elgar, S., Herbers, T.H.C., Guza, R.T., 1994. Reflection of ocean surface gravity waves from a natural beache. J. Phys. Oceanogr. 24, 1503–1511. https://doi.org/10.1175/1520-0485(1994)024.
Forte, M.F., Birkemeier, W.A., Mitchell, J.R., 2017. Nearshore Survey System Evaluation, pp. 1–46. ERDC/CHL TR-17-19.
Gomes da Silva, P., Coco, G., Garnier, R., Klein, A.H.F., 2020. On the prediction of runup, setup and swash on beaches. Earth Sci. Rev. 204 https://doi.org/10.1016/j.earscirev.2020.103148.
Gomes da Silva, P., Medina, R., González, M., Garnier, R., 2019. Wave reflection and saturation on natural beaches: the role of the morphodynamic beach state in incident swash. Coast. Eng. 153 https://doi.org/10.1016/j.coastaleng.2019.103540.
Grossmann, F., Hurther, D., Sánchez-arcilla, A., Alsina, J.M., 2023. Influence of the initial beach profile on the sediment transport processes during post-storm onshore bar migration journal of geophysical research : oceans. J. Geophys. Res. Oceans 128, 1–17. https://doi.org/10.1029/2022JC019299.
Hauser, D., Abdalla, S., Ardhuin, F., Bidlot, J.R., Bourassa, M., Cotton, D., Gommenginger, C., Evers-King, H., Johnsen, H., Knaff, J., Lavender, S., Mouche, A., Reul, N., Sampson, C., Steele, E.C.C., Stoffelen, A., 2023. Satellite remote sensing of surface winds, waves, and currents: where are we now? Surv. Geophys. https://doi.org/10.1007/s10712-023-09771-2.
Holman, R., Bergsma, E.W.J., 2021. Updates to and performance of the cbathy algorithm for estimating nearshore bathymetry from remote sensing imagery. Rem. Sens. 13 https://doi.org/10.3390/rs13193996.
Holman, R., Haller, M.C., 2013. Remote sensing of the nearshore. Ann. Rev. Mar. Sci 5, 95–113. https://doi.org/10.1146/annurev-marine-121211-172408.
Holman, R., Plant, N., Holland, T., 2013. CBathy: a robust algorithm for estimating nearshore bathymetry. J. Geophys. Res. Oceans 118, 2595–2609. https://doi.org/10.1002/jgrc.20199.
Honegger, D.A., Haller, M.C., Holman, R.A., 2019. High-resolution bathymetry estimates via X-band marine radar: 1. beaches. Coast. Eng. 149, 39–48. https://doi.org/10.1016/j.coastaleng.2019.03.003.
Hubbard, P.G., Vantassel, J.P., Cox, B.R., Rector, J.W., Yust, M.B.S., Soga, K., 2022. Quantifying the surface strain field induced by active sources with distributed acoustic sensing: theory and practice. Sensors 22, 4589. https://doi.org/10.3390/s22124589.
Huntley, D.A., Simmonds, D., Tatavarti, R., 1999. Use of collocated sensors to measure coastal wave reflection. J. Waterw. Port, Coast. Ocean Eng. 125, 46–52.
Ide, S., Araki, E., Matsumoto, H., 2021. Very broadband strain-rate measurements along a submarine fiber-optic cable off Cape Muroto, Nankai subduction zone, Japan. Earth Planets Space 73. https://doi.org/10.1186/s40623-021-01385-5.
Inch, K., Davidson, M., Masselink, G., Russell, P., 2017a. Correcting wave reflection estimates in the coastal zone. Coast. Eng. 119, 65–71. https://doi.org/10.1016/j.coastaleng.2016.09.004.
Inch, K., Davidson, M., Masselink, G., Russell, P., 2017b. Observations of nearshore infragravity wave dynamics under high energy swell and wind-wave conditions. Continent. Shelf Res. 138, 19–31. https://doi.org/10.1016/j.csr.2017.02.010.
Inch, K., Davidson, M., Masselink, G., Russell, P., 2016. Accurate estimation of wave reflection on a high energy, dissipative beach. In: Journal of Coastal Research. Coastal Education Research Foundation Inc., pp. 877–881. https://doi.org/10.2112/SI75-176.1
Jousset, P., Reinsch, T., Ryberg, T., Blanck, H., Clarke, A., Aghayev, R., Hersir, G.P., Henninges, J., Weber, M., Krawczyk, C.M., 2018. Dynamic strain determination using fibre-optic cables allows imaging of seismological and structural features. Nat. Commun. 9, 1–11. https://doi.org/10.1038/s41467-018-04860-y.
Landrø, M., Bouffaut, L., Kriesell, H.J., Potter, J.R., Rørstadbotnen, R.A., Taweesintananon, K., Johansen, S.E., Brenne, J.K., Haukanes, A., Schjelderup, O., Storvik, F., 2022. Sensing whales, storms, ships and earthquakes using an Arctic fibre optic cable. Sci. Rep. 12 https://doi.org/10.1038/s41598-022-23606-x.
Lin, C.Y., Huang, C.J., 2004. Decomposition of incident and reflected higher harmonic waves using four wave gauges. Coast. Eng. 51, 395–406. https://doi.org/10.1016/j.coastaleng.2004.04.004.
Lindsey, N.J., Dawe, T.C., Ajo-Franklin, J.B., 2019. Illuminating seafloor faults and ocean dynamics with dark fiber distributed acoustic sensing. Science 366, 1103–1107. https://doi.org/10.1126/science.aay5881, 1979.
Lindsey, N.J., Martin, E.R., 2021. Fiber-optic seismology. Annu. Rev. Earth Planet Sci. 49, 309–336. https://doi.org/10.1146/annurev-earth-072420-065213.
Lior, I., Sladen, A., Rivet, D., Ampuero, J.-P., Hello, Y., Becerril, C., Martins, H.F., Lamare, P., Jestin, C., Tsagkli, S., Markou, C., 2021. On the detection capabilities of underwater distributed acoustic sensing. J. Geophys. Res. Solid Earth 126, 1–20. https://doi.org/10.1029/2020JB020925.
Martin, E., 2018. Passive Imaging and Characterization of the Subsurface with Distributed Acoustic Sensing. Stanford University.
Martins, K., Blenkinsopp, C.E., Almar, R., Zang, J., 2017a. The influence of swash-based reflection on surf zone hydrodynamics: a wave-by-wave approach. Coast. Eng. 122, 27–43. https://doi.org/10.1016/j.coastaleng.2017.01.006.
Martins, K., Blenkinsopp, C.E., Power, H.E., Bruder, B., Puleo, J.A., Bergsma, E.W.J., 2017b. High-resolution monitoring of wave transformation in the surf zone using a LiDAR scanner array. Coast. Eng. 128, 37–43. https://doi.org/10.1016/j.coastaleng.2017.07.007.
Martins, K., Bonneton, P., de Viron, O., Turner, I.L., Harley, M.D., Splinter, K., 2023. New perspectives for nonlinear depth-inversion of the nearshore using boussinesq theory. Geophys. Res. Lett. 50, 1–10. https://doi.org/10.1029/2022GL100498.
Martins, K., Bonneton, P., Mouragues, A., Castelle, B., 2020. Non-hydrostatic, non-linear processes in the surf zone. J. Geophys. Res. Oceans 125, 1–21. https://doi.org/10.1029/2019JC015521.
Masselink, G., 1998. Field investigation of wave propagation over a bar and the consequent generation of secondary waves. Coast. Eng. 33, 1–9.
Mateeva, A., Lopez, J., Potters, H., Mestayer, J., Cox, B., Kiyashchenko, D., Wills, P., Grandi, S., Hornman, K., Kuvshinov, B., Berlang, W., Yang, Z., Detomo, R., 2014. Distributed acoustic sensing for reservoir monitoring with vertical seismic profiling. Geophys. Prospect. 62, 679–692. https://doi.org/10.1111/1365-2478.12116.
Matsumoto, H., Araki, E., Kimura, T., Fujie, G., Shiraishi, K., Tonegawa, T., Obana, K., Arai, R., Kaiho, Y., Nakamura, Y., Yokobiki, T., Kodaira, S., Takahashi, N., Ellwood, R., Yartsev, V., Karrenbach, M., 2021. Detection of hydroacoustic signals on a fiber-optic submarine cable. Sci. Rep. 11 https://doi.org/10.1038/s41598-021-82093-8.
Mecozzi, A., Cantono, M., Castellanos, J.C., Kamalov, V., Muller, R., Zhan, Z., 2021. Polarization sensing using submarine optical cables. Optica 8, 788. https://doi.org/10.1364/optica.424307.
Melito, L., Parlagreco, L., Devoti, S., Brocchini, M., 2022. Wave- and tide-induced infragravity dynamics at an intermediate-to-dissipative microtidal beach. J. Geophys. Res. Oceans 127. https://doi.org/10.1029/2021JC017980.
Mull, J., Ruggiero, P., Mult, J., Ruggiero, P., 2014. Estimating storm-induced dune erosion and overtopping along U.S. west coast beaches. J. Coast Res. 30, 1173–1187. https://doi.org/10.2112/JCOASTRES-D-13-00178.1.
Norheim, C.A., Herbers, T.H.C., Elgar, S., 1998. Nonlinear evolution of surface wave spectra on a beach. J. Phys. Oceanogr. 28, 1534–1551. https://doi.org/10.1175/1520-0485(1998)028<1534:NEOSWS>2.0.CO;2.
Nortek, 2022. The Comprehensive Manual for Velocimeters.
O'Dea, A., Brodie, K.L., Hartzell, P., 2019. Continuous coastal monitoring with an automated terrestrial lidar scanner. J. Mar. Sci. Eng. 7 https://doi.org/10.3390/jmse7020037.
O'Grady, J.G., McInnes, K.L., Hemer, M.A., Hoeke, R.K., Stephenson, A.G., Colberg, F., 2019. Extreme water levels for Australian beaches using empirical equations for shoreline wave setup. J. Geophys. Res. Oceans 124, 5468–5484. https://doi.org/10.1029/2018JC014871.
Palmsten, M.L., Brodie, K.L., 2022. The coastal imaging research network (CIRN). Rem. Sens. https://doi.org/10.3390/rs14030453.
Palmsten, M.L., Holman, R.A., 2012. Laboratory investigation of dune erosion using stereo video. Coast. Eng. 60, 123–135. https://doi.org/10.1016/j.coastaleng.2011.09.003.
Peng, Y., Zhang, D., Fu, S., Yedili, N., Ma, Z., 2023. Method of precise sensing channel positioning for φ-OTDR based DAS. Meas. Sci. Technol. https://doi.org/10.1088/1361-6501/acb456.
Plant, N.G., Holman, R.A., Freilich, M.H., Birkemeier, W.A., 1999. A simple model for interannual sandbar behavior. J. Geophys. Res. Oceans 104, 15755–15776. https://doi.org/10.1029/1999jc900112.
Reinsch, T., Thurley, T., Jousset, P., 2017. On the mechanical coupling of a fiber optic cable used for distributed acoustic/vibration sensing applications - a theoretical consideration. Meas. Sci. Technol. 28 https://doi.org/10.1088/1361-6501/aa8ba4.
Ruggiero, P., Komar, P.D., McDougal, W.G., Marra, J.J., Beach, R.A., 2001a. Wave runup, extreme water levels and the erosion of properties backing beaches. J. Coast Res. 17, 407–419. https://doi.org/10.1016/0049-3848(90)90038-E.
Ruggiero, P., Komar, P.D., McDougal, W.G., Marra, J.J., Beach, R.A., 2001b. Wave runup, extreme water levels and the erosion of properties backing beaches. J. Coast Res. 17, 407–419. https://doi.org/10.1016/0049-3848(90)90038-E.
Saprykina, Y., Kuznetsov, S., 2022. Cascade downshifting of peak frequency at wave spectra evolution on mild bottom slope: experimental investigations. Ocean. Eng. 259, 111958 https://doi.org/10.1016/j.oceaneng.2022.111958.
Senechal, N., Bonneton, P., Dupuis, H., 2002. Field experiment on secondary wave generation on a barred beach and the consequent evolution of energy dissipation on the beach face. Coast. Eng. 46, 233–247.
Senechal, N., Coco, G., Bryan, K.R., Holman, R.A., 2011. Wave runup during extreme storm conditions. J. Geophys. Res. Oceans 116, 1–13. https://doi.org/10.1029/2010JC006819.
Serafin, K.A., Ruggiero, P., Barnard, P.L., Stockdon, H.F., 2019. The influence of shelf bathymetry and beach topography on extreme total water levels: linking large-scale

changes of the wave climate to local coastal hazards. Coast. Eng. 150, 1–17. https://doi.org/10.1016/j.coastaleng.2019.03.012.
Sheremet, A., Guza, R.T., Elgar, S., Herbers, T.H.C., 2002. Observations of nearshore infragravity waves: seaward and shoreward propagating components. J. Geophys. Res. Oceans 107. https://doi.org/10.1029/2001jc000970.
Sheremet, A., Staples, T., Ardhuin, F., Suanez, S., Fichaut, B., 2014. Observations of large infragravity wave runup at Banneg Island, France. Geophys. Res. Lett. 41, 976–982. https://doi.org/10.1002/2013GL058880.
Sidenko, E., Tertyshnikov, K., Lebedev, M., Pevzner, R., 2022. Experimental study of temperature change effect on distributed acoustic sensing continuous measurements. Geophysics 87, 111–122. https://doi.org/10.1190/geo2021-0524.1.
Smith, M.M., Thomson, J., Baker, M.G., Abbott, R.E., Davis, J., 2023. Observations of ocean surface wave attenuation in sea ice using seafloor cables. Geophys. Res. Lett. 50 https://doi.org/10.1029/2023GL105243.
Spica, Z.J., Castellanos, J.C., Viens, L., Nishida, K., Akuhara, T., Shinohara, M., Yamada, T., 2022. Subsurface imaging with ocean-bottom distributed acoustic sensing and water phases reverberations. Geophys. Res. Lett. 49, 1–11. https://doi.org/10.1029/2021GL095287.
Spica, Z.J., Nishida, K., Akuhara, T., Pétrélis, F., Shinohara, M., Yamada, T., 2020. Marine sediment characterized by ocean-bottom fiber-optic seismology. Geophys. Res. Lett. 47, 1–10. https://doi.org/10.1029/2020GL088360.
Splinter, K.D., Harley, M.D., Turner, I.L., 2018. Remote sensing is changing our view of the coast: insights from 40 years of monitoring at Narrabeen-Collaroy, Australias. Rem. Sens. 10 https://doi.org/10.3390/rs10111744.
Streßer, M., Horstmann, J., Baschek, B., 2022. Surface wave and roller dissipation observed with shore-based Doppler marine radar. J. Geophys. Res. Oceans 127, 1–22. https://doi.org/10.1029/2022JC018437.
Taweesintananon, K., Landrø, M., Brenne, J.K., Haukanes, A., 2021. Distributed acoustic sensing for near-surface imaging using submarine telecommunication cable: a case study in the Trondheimsfjord, Norway. Geophysics 86, 303–320. https://doi.org/10.1190/geo2020-0834.1.
Taweesintananon, K., Landrø, M., Potter, J.R., Johansen, S.E., Rørstadbotnen, R.A., Bouffaut, L., Kriesell, H.J., Brenne, J.K., Haukanes, A., Schjelderup, O., Storvik, F., 2023. Distributed acoustic sensing of ocean-bottom seismo-acoustics and distant storms: a case study from Svalbard, Norway. Geophysics 1–65. https://doi.org/10.1190/geo2022-0435.1.
Thomson, J., Elgar, S., Raubenheimer, B., Herbers, T.H.C., Guza, R.T., 2006. Tidal modulation of infragravity waves via nonlinear energy losses in the surfzone. Geophys. Res. Lett. 33 https://doi.org/10.1029/2005GL025514.
Traer, J., Gerstoft, P., Bromirski, P.D., Shearer, P.M., 2012. Microseisms and hum from ocean surface gravity waves. J. Geophys. Res. Solid Earth 117. https://doi.org/10.1029/2012JB009550.
Ugalde, A., Becerril, C., Villaseñor, A., Ranero, C.R., Fernández-Ruiz, M.R., Martin-Lopez, S., González-Herráez, M., Martins, H.F., 2022. Noise levels and signals observed on submarine fibers in the canary islands using DAS. Seismol Res. Lett. 93, 351–363. https://doi.org/10.1785/0220210049.
USACE, 2023. CHL data server [WWW Document]. URL. https://chlthredds.erdc.dren.mil/thredds/catalog/frf/catalog.html.
Vantassel, J.P., Cox, B.R., Hubbard, P.G., Yust, M., 2022. Extracting high-resolution, multi-mode surface wave dispersion data from distributed acoustic sensing measurements using the multichannel analysis of surface waves. J. Appl. Geophys. 205, 1–13. https://doi.org/10.1016/j.jappgeo.2022.104776.
Viens, L., Bonilla, L.F., Spica, Z.J., Nishida, K., Yamada, T., Shinohara, M., 2022. Nonlinear earthquake response of marine sediments with distributed acoustic sensing. Geophys. Res. Lett. 49, 1–12. https://doi.org/10.1029/2022gl100122.
Williams, Ethan F., Fernández-Ruiz, María R., Magalhaes, Regina, Vanthillo, Roel, Zhan, Zhongwen, González-Herráez, Miguel, Martins, Hugo F., 2019. Distributed sensing of microseisms and teleseisms with submarine dark fibers. Nat. Commun. 10 https://doi.org/10.1038/s41467-019-13262-7.
Williams, Ethan F., Zhan, Zhongwen, Martins, Hugo F., Fernández-Ruiz, María R., Martín-López, Sonia, González-Herráez, Miguel, Callies, Jörn, 2022. Surface gravity wave interferometry and ocean current monitoring with ocean-bottom das. J. Geophys. Res. Oceans 127, 1–27. https://doi.org/10.1029/2021jc018375.
Wilson, G.W., Özkan-Haller, H.T., Holman, R.A., Haller, M.C., Honegger, D.A., Chickadel, C.C., 2014. Surf zone bathymetry and circulation predictions via data assimilation of remote sensing observations. J. Geophys. Res. Oceans 119, 1993–2016. https://doi.org/10.1002/2013JC009213.
Zelt, J.A., Skjelbreia, J.E., 1992. Estimating incident and reflected wave fields using an arbitrary number of wave gauges. In: Proceedings of the 23rd Conference on Coastal Engineering, Venice, Italy, pp. 777–789.
Zhang, C., Li, Y., Zheng, J., Xie, M., Shi, J., Wang, G., 2021. Parametric modelling of nearshore wave reflection. Coast. Eng. 169, 103978 https://doi.org/10.1016/j.coastaleng.2021.103978.